Journal of Catalysis 277 (2011) 134–148

Contents lists available at ScienceDirect

Journal of Catalysis

journal homepage: www.elsevier.com/locate/jcat

Modeling spatially resolved data of methane catalytic partial oxidation on Rh foam catalyst at different inlet compositions and flowrates

D. Dalle Nogare [a,*], N.J. Degenstein [b], R. Horn [c], P. Canu [a], L.D. Schmidt [b]

[a] Dep. of Chemical Engineering Principles and Practice, Università di Padova, Via Marzolo, 9, 35131 Padova, Italy
[b] Dep. of Chemical Engineering and Materials Science, University of Minnesota, 432 Amundson Hall, 421 Washington Avenue SE, Minneapolis, MN 55455, USA
[c] Dep. of Inorganic Chemistry, Fritz-Haber-Institute of the Max-Planck-Society, Faradayweg 4-6, Berlin 14195, Germany

ARTICLE INFO

Article history:
Received 22 June 2010
Revised 28 October 2010
Accepted 28 October 2010
Available online 13 December 2010

Keywords:
Syngas
Catalytic partial oxidation
Methane
Rhodium
Spatial profiles
Mass transport
Detailed kinetics
Reactor modeling
Foam catalysts

ABSTRACT

Spatially resolved species and temperature profiles measured for a wide range of inlet stoichiometries and flowrates are compared with microkinetic numerical simulations to investigate the effect of transport phenomena on the catalytic partial oxidation of methane on Rh foam catalysts. In agreement with the experimental data, the species profiles calculated at different C/O inlet stoichiometries show that both partial oxidation products (H_2, CO) and total oxidation products (H_2O, CO_2) are formed in the presence of oxygen. At the leaner stoichiometries, both oxygen and methane react in the diffusive regime at the catalyst entrance. At the richest methane stoichiometry (high C/O), surface temperatures are lower and methane consumption is only partly determined by transport. For all stoichiometries, a kinetically controlled regime prevails in the downstream reforming zone after O_2 is fully consumed. The effect of increasing the flowrate shifts all species profiles downstream and also slightly modifies the shapes of the axial profiles, due to the different effectiveness of heat and mass transfer. Despite enhanced mass transfer and increased surface temperature, the shortened contact time causes a reduced CH_4 conversion at high flowrates. The effect of flowrate on the dominant regime is investigated, for both reactants, comparing the resistances calculated in the pure transport regime and in the pure kinetic regime. From a chemical point of view, the model allows for the analysis of the reaction path leading to hydrogen. Due to inhibition of H_2O re-adsorption, it can be proven that H_2 can be a primary product even in the presence of gas phase O_2. The analysis of the surface coverages shows analogous effects on the profiles when decreasing C/O or increasing flow, because in both cases the surface temperature is increased. Syngas selectivity was also evaluated, both from measured and calculated profiles. S_{H2} is well described by the model at each stoichiometry and flowrate, while S_{CO} is underestimated in every case. From this work, it is also indicated that the Rh catalyst works with CO (measured) selectivities higher than equilibrium. Carbon dioxide only forms in the oxidation zone, for C/O = 1 and 1.3, but in the rest of the catalyst zone, there is no further production despite what would be expected from equilibrium. This confirms Rh does not catalyze the water gas shift reaction. On the other hand, at C/O = 0.8, this reaction becomes active, due to the higher temperature, and the CO_2 is also produced in the reforming zone. This suggests that CO_2 will not rise after the oxidation section if the surface temperature is kept sufficiently low. Sensitivity analyses to the active catalytic surface and to the kinetic parameters are provided.

1. Introduction

Methane catalytic partial oxidation (CPO) to synthesis gas is an alternative to other energy-intensive technologies for industrial exploitation of natural gas. Its optimal utilization requires a deep insight into the underlying chemistry. Even though the reaction has been investigated for the past two decades [1–5], there are still open questions and further scientific investigation is required. Methane oxidation kinetics are very complicated, yet they are the simplest among the hydrocarbon oxidation processes. Since both exothermic and endothermic reactions are involved, a temperature variation does not translate directly to a reactant conversion, and energy and mass balances are deeply coupled. Therefore, CPO is a challenging and fascinating application where chemistry and transport phenomena are intrinsically connected with each other, determining the final product distribution. Appropriate modeling is needed to reproduce these complex features and to derive a molecular understanding of the reaction mechanism.

* Corresponding author. Fax: +39 049 827 5461.
E-mail addresses: daniela.dallenogare@unipd.it (D. Dalle Nogare), horn_r@fhi-berlin.mpg.de (R. Horn), paolo.canu@unipd.it (P. Canu), schmi001@umn.edu (L.D. Schmidt).

0021-9517/$ - see front matter © 2010 Elsevier Inc. All rights reserved.
doi:10.1016/j.jcat.2010.10.020

Nomenclature

bold	vectors
•	free surface site
c_i	concentration, kmol m^{-3}
c_P	bulk gas specific heat, J kg^{-1} K^{-1}
$c_{P,S}$	solid specific heat, J kg^{-1} K^{-1}
D_i	species molecular diffusivity, m^2 s^{-1}
dpore	pore diameter, m
f	tortuosity factor
h	species enthalpy, J $kmol_i^{-1}$
ΔH_R	enthalpy of reaction, J $kmol^{-1}$
K_I^*	pseudo-first-order kinetic constant, m s^{-1}
K	extinction coefficient, m^{-1}
K_C	mass transfer coefficient, m s^{-1}
K_T	heat transfer coefficient, W m^{-2} K^{-1}
L	each monolith length, m
Nsp	number of chemical species
$\dot{S}$	species production rate by surface reaction, $kmol_i$ m^{-2} s^{-1}
S_V	geometric surface to void volume, $S_V = 4/\text{dpore}$, m^{-1}
S'_V	geometric surface to bed volume, $S'_V = S_V\varepsilon$, m^{-1}
$S_{V,C}$	active catalytic surface to void volume, m^{-1}
t	time, s
T_G	bulk gas temperature, K
T_S	solid temperature, K
v	interstitial velocity, m s^{-1}
W	molar mass, kg_i $kmol_i^{-1}$
X_{CH4}	methane conversion
Y_G	bulk mass fractions, kg_i/kg_{tot}
Y_{BL}	BL mass fractions, kg_i/kg_{tot}
z	axial coordinate, m

Greek letters

ε	foam porosity, V_{void}/V_{bed}
η	viscosity, kg m^{-1} s^{-1}
λ_G	bulk gas thermal conductivity, W m^{-1} K^{-1}
λ_S	solid thermal conductivity, W m^{-1} K^{-1}
ρ_G	bulk gas density, kg m^{-3}
ρ_{BL}	boundary layer gas density, kg m^{-3}
ρ_S	solid density, kg m^{-3}

Dimensionless numbers

Pe_M	Re·Sc
Pe_T	Re·Pr
Pr	$\frac{\eta \cdot C_P}{\lambda}$
Re	$\frac{G}{\eta S_V}$
Sc	$\frac{\eta}{\rho \cdot D}$

Although there are many possible elementary reactions in the methane CPO system, the number of global reactions which may take place is not that high because the system is constrained to give only six products: CH_4, CO_2, CO, H_2, H_2O and O_2 (higher hydrocarbons are commonly not detected). Some of the possible exothermic oxidation reactions ranging from total oxidation to partial oxidation are listed below.

Total Oxidation: $CH_4 + 2O_2 = 2H_2O + CO_2$

$$\Delta H_R^{298} = -803 \text{ kJ mol}^{-1} \quad \text{(R1)}$$

Partial Oxidation to H_2O and syngas:

$$CH_4 + O_2 = H_2 + CO + H_2O \quad \Delta H_R^{298} = -278 \text{ kJ mol}^{-1} \quad \text{(R2)}$$

Partial Oxidation to Syngas: $CH_4 + 1/2O_2 = 2H_2 + CO$

$$\Delta H_R^{298} = -36 \text{ kJ mol}^{-1} \quad \text{(R3)}$$

After oxygen is consumed, there are only three global reactions which can take place (only two of them independent): steam reforming (SR), water gas shift (WGS) and dry reforming (DR), even if there is experimental evidence that DR does not occur on Rh and is a result of the combination of SR and WGS [6–9].

Steam Reforming: $CH_4 + H_2O = 3H_2 + CO$

$$\Delta H_R^{298} = +206 \text{ kJ mol}^{-1} \quad \text{(R4)}$$

Water Gas Shift: $H_2O + CO = H_2 + CO_2$

$$\Delta H_R^{298} = -41 \text{ kJ mol}^{-1} \quad \text{(R5)}$$

Dry Reforming: $CH_4 + CO_2 = 2H_2 + 2CO$

$$\Delta H_R^{298} = +247 \text{ kJ mol}^{-1} \quad \text{(R6)}$$

The interplay between chemical and physical processes has been acknowledged to be a fundamental issue in the modeling [10,11] of fast, exothermic reactions. Plug flow reactor (PFR) models are unsatisfactory for catalytic combustion applications because of the excessive simplifications in heat and mass transport; full computational fluid dynamics (CFD) models or at least lumped models accounting for transport phenomena [12–14] are required.

The reaction rate of species involved in very fast reactions will be dominated by the system's mass transfer characteristics. However, for the other slower reactions, a good kinetic model and accurate assumption for active surface area are required. It is obvious that for an optimal kinetic study, all the species should be in kinetic control and also a safe determination of the reaction (surface) temperature is necessary. Only if the temperature is well captured by the model is a proper kinetic study possible. The dominant regime is investigated for oxygen and methane, at every flowrate, comparing the mass transfer coefficient and the kinetic constant of the pseudo-first-order reaction, i.e. the consumption rate divided by the concentration.

The reaction path influences and is in turn influenced by the temperature profile. This means that even if chemical kinetics are accurately described, incorrect species profiles will result unless a suitable temperature profile is used. However, the latter is not easy to model, because it is affected simultaneously by several physical transport processes. Heat released by the reaction [15] is transported by gas convection and conduction (minor gas phase influence of radiation) and solid conduction and radiation. Given the exponential temperature dependence of the kinetics on the one hand and the complexity of the phenomena contributing to the heat balance on the other hand, the kinetics will be more influenced by the temperature profile than vice versa. Therefore, a model capable of reproducing the temperature profile will reasonably predict species profiles, in particular far from the catalyst entrance.

At relatively long residence times, the kinetics slow down and the exit composition approaches equilibrium, which depends only on temperature. The authors showed [14] that also the PFR model correctly describes the exit composition, with the correct exit temperature, even if the onset of the calculated profiles diverges greatly from the experimental data at the inlet of the catalyst.

Several studies have been published where a good description of the temperature profile led to a reasonable prediction of gas products, even without accounting for mass transfer limitations ([16] and partly in [17]) or for a detailed kinetic scheme [18–20]. On the other side, [21] provides an example of detailed modeling, accounting for both mass transfer and kinetics, that shows disagreement between calculated and measured product distribution, at the early stage of ignition, as well as of the temperature, presumably because of an inaccurate description of the energy balance. In our previous work [14], some underestimation of the solid temperature in the oxidation zone might be contributing to an underestimation of CO selectivity, which indeed increases with higher surface temperature [16]. This effect of temperature on CO selectivity is the combined result of a rapid desorption of CO and a low concentration of gas phase O_2 at the catalyst surface due to transport resistances in the film, which could cause irreversible further oxidation to CO_2. CO_2 has a very low probability to re-adsorb on the surface and to dissociate back into $CO_{(s)}$ and $O_{(s)}$, which is reflected in the used mechanism by the very low sticking coefficient. As a consequence, CO_2 reforming is rather unlikely and a direct path can be postulated for CO production. Contrary to CO_2, water has a high probability to adsorb and react in the steam reforming reaction, so that both direct and indirect paths are possible. The route to hydrogen is one of the open issues that has been investigated over the years and will be discussed in light of the results available from the model. In the present work, we use the same model as in [14] to describe the profiles at different stoichiometries and flowrates and provide an additional sensitivity analysis on the most uncertain parameters, which are the catalytically active surface-to-volume ratio and the kinetic constants of the surface mechanism.

2. Experimental data

The reactor setup to measure spatially resolved species and temperature data was presented in detail in a previous work [22]. Composition profiles of species CH_4, CO, CO_2, H_2 and O_2 were measured with a capillary sampling technique and mass spectrometry (MS). The H_2O profile was not measured; it was obtained from H and O balances, using a mean square error technique. Since the continuity equation can be applied to every single atomic species, both differences in the H and O atom balance can be accounted for by H_2O molecules. The H_2O local concentration was then estimated as the value that minimizes the residual sum of squares of the errors in both H and O mass balances, at each axial measurement. The catalyst foam was an 80 ppi α-alumina foam coated with 5 wt% rhodium. A washcoat was not applied, and the noble metal was deposited directly on the nonporous α-alumina. The catalyst foam was sandwiched between two uncoated 80 ppi α-alumina foam monoliths serving as heat shields before and after the catalyst, all of them being 10 mm long. The preheat temperature of the gases flowing into the front heat shield monolith was 100 °C. In addition, the reactor was well insulated in the radial direction and behaved almost adiabatically. The enthalpy of the gas mixture exiting the back heat shield, which is a function of measured temperature and composition, was equal to the enthalpy of the gas mixture entering the front heat shield, within 5% error.

Experiments presented in this work include the influence of inlet stoichiometry (C/O ratio) and flowrate (F), not previously investigated. The C/O ratio stands here for the ratio of carbon to oxygen atoms in the feed gas. Data for C/O = 1 (syngas stoichiometry, R3) and F = 5 slpm were presented and compared with a numerical model in an earlier work [14] and serve here solely as a point of reference for evaluating the new data at different stoichiometries and flowrates. Two new data sets were produced by the authors [23], one varying C/O = [0.8, 1, 1.3] at F = 5 slpm and the other increasing F = [2.5, 5, 7.5, 10] slpm at C/O = 1 and are compared here with the profiles calculated by the same numerical model. For all experiments, argon was used as inert carrier and internal standard for the MS quantification to prevent signal conflict between N_2 and CO at m/z = 28 amu. The argon-to-oxygen ratio was 3.76:1 in all experiments to match the N_2-to-O_2 ratio typical of air. Temperature profiles were available only for the experiments at different C/O.

2.1. Experimental profiles at reference C/O = 1 and flowrate F = 5 slpm

Data at C/O = 1 and 5 slpm are presented in Fig. 1; all species profiles are included to show how the species evolve relative to each other. As this picture is qualitatively the same for all conditions investigated, the species profiles are not presented altogether in all subsequent figures but are split into two groups (top: H_2, CH_4, O_2 and bottom: CO, H_2O, CO_2). Reactants, CH_4 and O_2, go through the front heat shield unconverted. The bending of their profiles close to the catalyst entrance is due to diffusive fluxes driven by the strong concentration gradients in the reacting zone, as typical of flame fronts [24]. Oxygen is totally consumed within the first 3 mm of the catalyst foam, which will be called "oxidation zone". In an earlier work, we proved that O_2 reacts in full mass transfer limitation in this zone [25]. The 1:1 reactant conversion within the first mm of the catalyst foam can approximately be described as partial oxidation of methane to H_2O and syngas (R2) even though the feed stoichiometry (C/O = 1) corresponds to partial oxidation to syngas stoichiometry. All products (H_2, CO, H_2O and CO_2) are formed in the oxidation zone. Later downstream, H_2O is consumed, further reacting with CH_4 in the SR reaction (R4) and, possibly, with CO in the WGS reaction (R5). After O_2 is largely consumed ($z \approx 0.011$ m), the slope of CH_4 decreases. Methane consumption continues behind the point of complete O_2 consumption by reaction with H_2O to CO and H_2 in a ratio of 1:3 reflecting steam reforming stoichiometry (R4). This zone will be called "reforming zone". CO_2 has a net production rate only in the early oxidation zone, probably because the fraction of active sites covered by oxygen atoms is relatively high (above 0.1%, see Fig. 17) in this catalyst section and the surface temperature (see Fig. 3) reaches values above 1000 °C. Dry reforming (R6) which should lead to a net consumption of CO_2 is not seen to occur at these conditions. H_2 and CO are produced throughout the catalyst bed, at the beginning in a 1:1 ratio in agreement with (R2), but from $z \approx 0.01$ m onward, the ratio turns to 3:1 as for steam reforming (R4), reducing to approximately

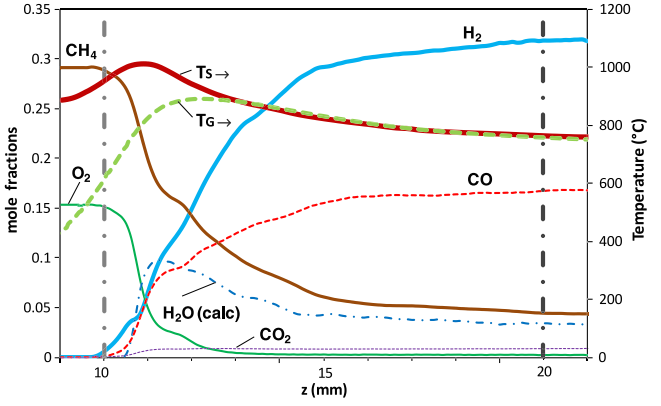

Fig. 1. Experimental species and temperature profiles at C/O = 1.0 and F = 5 slpm total flowrate. H_2O is a calculated profile. The abscissa denotes positions in the reactor bed. The catalyst spans from 10 mm to 20 mm. Regions z < 10 mm and z > 20 mm are in the front and back heat shield, respectively.

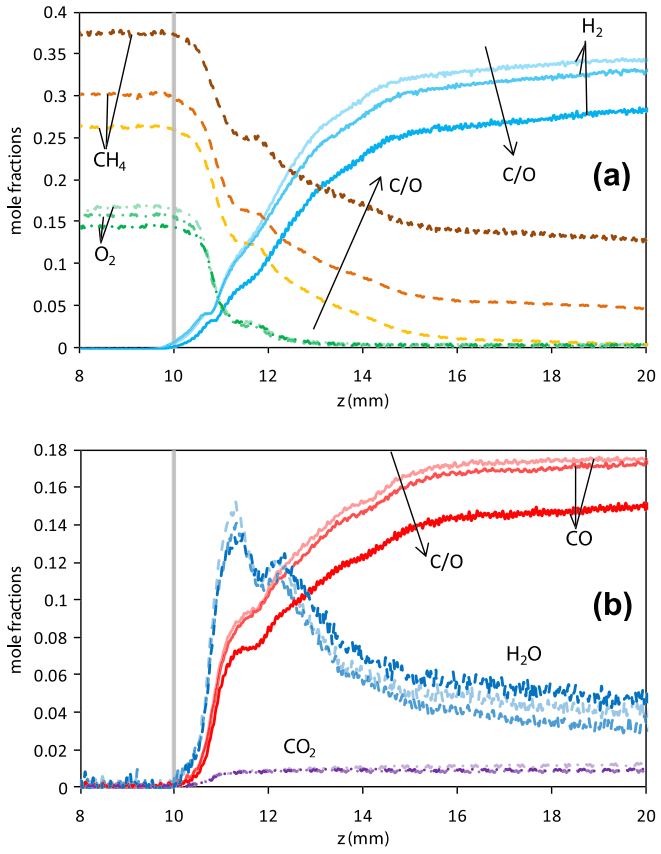

Fig. 2. Experimental species profiles at total inlet flowrate F = 5 slpm and C/O = 0.8, 1.0, 1.3 stoichiometry (lighter to darker color). H_2O is a calculated profile. CH_4, O_2 and H_2 mole fractions (panel a), CO, H_2O and CO_2 (panel b). The catalyst section spans from 10 mm to 20 mm.

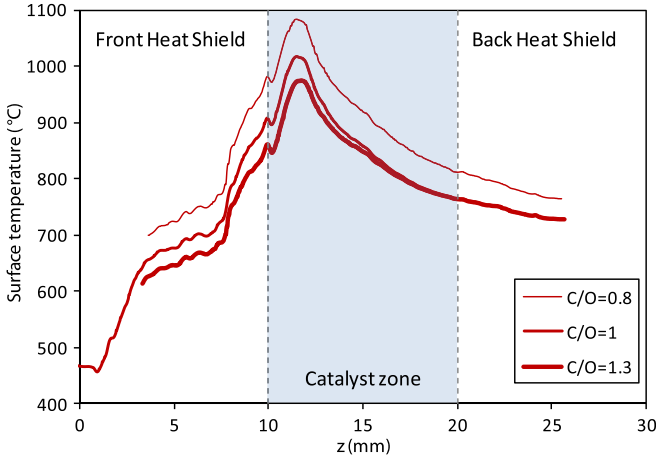

Fig. 3. Pyrometer measurements of surface temperature profiles at total inlet flowrate F = 5 slpm and C/O = 0.8, 1, 1.3 stoichiometry (thinner to thicker line). The displayed abscissa spans from the entrance of the front heat shield to the end of the back heat shield, 0 mm to 30 mm. The catalyst zone, from 10 mm to 20 mm, is highlighted.

2:1 at the end of the catalyst, as expected from syngas formation by CPO (R3). The significant amount of syngas produced in the oxidation zone might suggest that the mechanism is direct, but from the analysis of the species profiles in the gas film contacting the catalyst, as accessible from model, water is available as reactant early on in the catalyst, making the indirect syngas formation path via steam reforming quite likely. At C/O = 1, thermodynamic equilibrium allows 87% methane conversion, which is slightly higher than the experimental value of 80%. Despite the rapid O_2 conversion within the first few millimeters of the catalyst foam, the reactions in the reforming zone are too slow to reach equilibrium CH_4 conversion at the actual residence time and available catalytic surface area (no washcoat applied). The endothermic SR reaction (R4) with its high activation energy runs indeed faster in the oxidation where heat is continuously produced than in the reforming zone where SR continuously lowers the catalyst temperature. The species concentrations remain approximately constant in the back heat shield, where axial diffusion is not supported by significant gradients. For these reasons, all the following figures will not report the back heat shield.

It should be noticed that small bumps and discontinuities are sometimes apparent in the profile data. There is a short latent zone in the first 0.5 mm (one pore length) of the catalyst, in which the kinetics seem to be unexpectedly slow; just before 12 mm, we measured a small bump in the methane and oxygen curves, and so on. We believe that these artifacts are due to the irregular structure of the support, alternating empty and filled spaces and producing intricate flow patterns, and do not have other physical or chemical explanation requiring the model to account for them.

The same figure shows the temperature profiles, read by the thermocouple (T_G) and the pyrometer (T_S). Surface temperature is higher than gas temperature in the oxidation zone, due to the strong heat release from the oxidation reactions (R1)–(R3). The difference between the two temperatures, up to 300 °C, reaffirms the presence of transfer phenomena in the first millimeters of the catalyst, where the kinetics is fast. At the end of the oxidation zone, the temperature profiles cross, because endothermic reactions are occurring on the surface. However, since the kinetics of steam reforming are very slow, there is no more transfer resistance, and the two temperatures overlap.

2.2. Experimental profiles at different C/O

Experiments at different inlet compositions were carried out at the reference flowrate of 5 slpm. The Ar/O_2 ratio was kept constant at 3.76. Therefore, each C/O ratio corresponds to a particular set of inlet flows of CH_4, O_2 and Ar. Fig. 2 shows the species profiles at three different inlet stoichiometries, C/O = 0.8, 1.0 and 1.3.

The same general features are present for all three stoichiometries. Oxygen is known to react with a pseudo-first-order kinetics [25], due to strong transfer limitations in the early oxidation zone. This is indeed reflected in Fig. 2 in such a way that early in the oxidation zone, the O_2 profiles start from different values but shortly join together, revealing a faster decrease for the highest concentration. As the number of moles (total inlet flow) was kept constant, the concentration is the same from this point on and the O_2 profiles decline simultaneously and exponentially to zero. Methane reacts throughout the reactor with slightly different consumption rates. The numerical differentiation of the profiles in the axial direction shows the trend $r_{CH4}^{C/O=0.8} > r_{CH4}^{C/O=1} > r_{CH4}^{C/O=1.3}$. This can be rationalized by taking into account that the temperature level follows the same trend ($T_S^{C/O=0.8} > T_S^{C/O=1} > T_S^{C/O=1.3}$), Fig. 3) and that temperature has a major effect on the rate of CH_4 consumption both in diffusive regime ($K_c \propto T^{1.75}$) and in kinetic regime. Water and CO_2 profiles are very similar in all cases especially with regard to location and height of the water peaks. The water maximum is higher for C/O = 0.8, consistently with a higher O_2 mole fraction in the feed. Due to the higher temperature levels for C/O = 0.8 and 1.0, H_2O consumption is faster for these stoichiometries than for the C/O = 1.3. The CO_2 profiles are nearly identical for C/O = 1.3 and C/O = 1 and only slightly higher for C/O = 0.8. Interestingly, the

higher production of CO_2 does not occur in the oxidation zone, as could be expected due to a higher O_2 concentration in the feed, but CO_2 is produced also in the reforming/WGS region of the reactor, possibly because of a very high surface temperature. Together with a higher H_2O production at lower C/O, there is a higher H_2 production, as well. This again indicates that higher temperatures favor the SR (R4) reaction, as already noticed in terms of a higher CH_4 consumption. C/O = 0.8 and C/O = 1 reach similar syngas levels at the exit of the catalyst, whereas for C/O = 1.3, the exit level is much lower. This indicates that the former two cases suffer mass transfer limitation also for methane, while the latter is in kinetic control. From these experimental findings, it can be deduced that CH_4 is mass transfer controlled for the leanest mixtures, while for the richer (C/O = 1.3), the regime is mixed, because the kinetics are slowed down by the lower T. In the reforming zone, surface reactions, which are no longer fully mass transfer controlled as in the oxidation zone, proceed at slower rates leading to a differentiation in all the species also for the C/O = 0.8 and C/O = 1.0 stoichiometries.

By observing the effects of different stoichiometries on the composition, it can be noticed that the total oxidation always occurs at the beginning, consuming O_2 as fast as it can; a higher C/O ratio is unfavorable for the endothermic reforming reaction, because of the lower catalyst temperature; in the reforming zone, there is some WGS (R5) reaction, relevant only at the highest C/O.

Not only does the temperature influence the kinetics, but also the vice versa is true. The relatively high amount of oxidant at the lower C/O implies a stronger heat release in the oxidation zone, with a consequent higher surface temperature (Fig. 3). On the other hand, in the C/O = 1.3 case, the SR (R4) is slower and adsorbs a smaller amount of heat than in the other stoichiometries. Therefore, the temperature decrease is less steep and eventually the surface temperature profiles overlap for C/O = 1 and 1.3.

2.3. Experimental profiles at different flowrates at C/O = 1.0

Flowrate variations between 2.5 and 10 slpm were used to investigate the dependence of the reaction on flowrate at the constant reference stoichiometry C/O = 1.0. Fig. 4 shows the species profiles for all flowrates investigated.

By increasing the flowrate, convection shifts all profiles downstream. It enhances the transport phenomena, but at the same time, it reduces the contact time in the reactor. The oxidation zone becomes longer, and the remaining reforming region shortens. From 2.5 to 10 slpm, methane conversion and syngas selectivity decrease. Obviously, the decreasing contact time affects mostly the relatively slow steam reforming reaction, which is mainly responsible for syngas production. Noticeably, the CO_2 production is almost the same even upon quadrupling the flowrate.

Mass and heat Péclet numbers (see nomenclature) estimate the ratio between convection and diffusion (or conduction). At the catalyst entrance (z = 0.01 m), we calculate, for the lower flowrate, Pe_{H2} = 0.25 and, for T and the other species, it spans a range from 0.7 to 1.3. For the largest flowrate used, Pe_{H2} = 1.1 and the other Pe's vary from 3 to 5.5. Consequently, axial diffusive and conductive fluxes are never negligible and sometimes prevail over convection. This affects both the modeling and the understanding of the experimental profiles. At 2.5 slpm, diffusion for all species and heat conduction in the gas phase has to be considered. Due to its small mass, H_2 diffuses particularly fast. At 10 slpm, convection is the dominant transport mechanism for all species but H_2 and temperature. Even at 10 slpm, H_2 can diffuse against the flow direction. Diffusion smoothes out all gradients in the profiles to some extent, in particular at the lower flowrates and in regions of larger gradients.

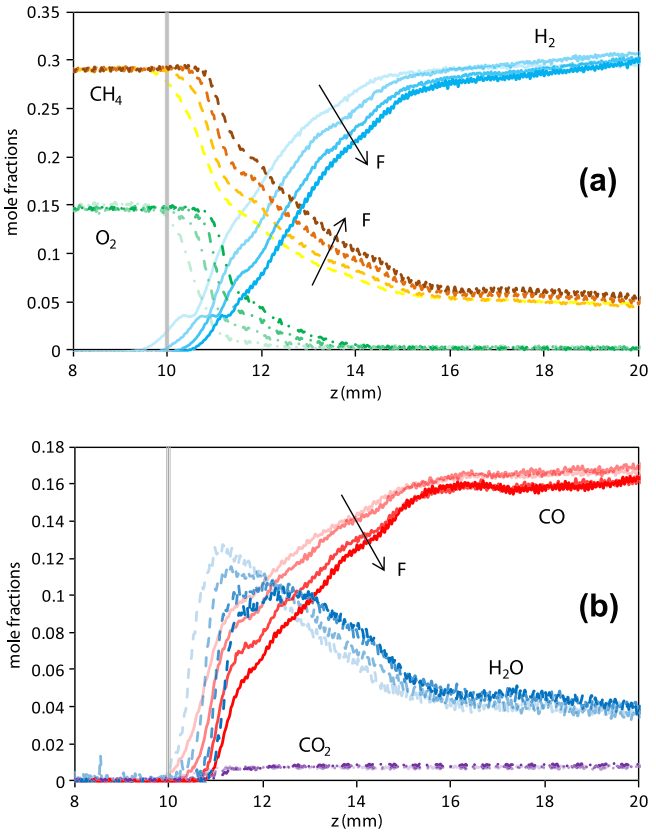

Fig. 4. Experimental species profiles at a feed stoichiometry of C/O = 1.0 and total inlet flowrates of F = 2.5, 5, 7.5, 10 slpm (lighter to darker color). H_2O is a calculated profile. CH_4, O_2 and H_2 mole fractions (panel a), CO, H_2O and CO_2 (panel b). The catalyst section spans from 10 mm to 20 mm.

3. Numerical modeling: results and discussion

Spatially resolved experimental data as presented previously present a unique opportunity to pointwise validate numerical predictions from detailed models. Recently, new reactor configurations allowed 2D/3D inspection of the catalysts [26,27], but for the first time, the described capillary sampling technique gave very high resolution species profiles in this geometry [28]. While it is certainly interesting and exciting to simply collect and discuss these profiles, the ability to compare experimental profiles with numerical simulations allows a deeper and more quantitative insight into the chemistry and its interaction with physical transport processes.

The model used in this work was already presented and validated for the reference case 5 slpm and C/O = 1 in a previous work. Considering the experimental artifacts in the species profiles and the uncertainty of some of the geometrical parameters of the model, the agreement was remarkable. The extended data presented in this work for different C/O ratios and flowrates allow to test the model further and to extract information about the interaction of chemistry and transport that are experimentally inaccessible.

3.1. Model equations

The reactor model, which includes transport phenomena, consists of transient, one-dimensional (axial) balances for heat (energy balance, EB) and species mass (mass balances, MBs). The momentum balance is not considered, since the pressure drop, evaluated with the Ergun equation, is negligible, even in this relatively dense foam [29]. From the continuity equation, the mass flux (ρv) is

constant. The reactor is represented as a straight channel, where the bulk gas phase has certain composition and properties, while there is a thin layer of gas (a film, or the boundary layer) close to the solid surface with its own composition and properties. In the following, the subscript G denotes quantities in the bulk gas phase, whereas the subscript BL refers to quantities in the boundary layer, in contact with the catalytic surface. At atmospheric pressure, the CPO kinetics are solely catalytic and homogeneous reactions in the gas phase can be neglected [30–33]. The composition in the bulk gas phase can be related to that in the BL through transfer coefficients of mass and heat, using a lumped model [12].

The equations are written on a void volume basis. Symbols are explained in the notation.

$$\text{Bulk MB:}\quad \rho_G\frac{\partial Y_G}{\partial t} = -\rho_G V\frac{\partial Y_G}{\partial z} + \rho_G D\frac{\partial^2 Y_G}{\partial z^2} - \rho_G S_V \boldsymbol{K}_C(\boldsymbol{Y}_G - \boldsymbol{Y}_{BL})\ \text{Nsp} = 7 \tag{1}$$

$$\text{BL MB:}\quad \rho_{BL}\frac{\partial Y_{BL}}{\partial t} = \rho_{BL} S_V \boldsymbol{K}_C(\boldsymbol{Y}_G - \boldsymbol{Y}_{BL}) + S_{V,C}\dot{\boldsymbol{s}}\cdot\boldsymbol{W}\ \text{Nsp} = 7 \tag{2}$$

$$\text{Bulk EB:}\quad \rho_G C_p\frac{\partial T_G}{\partial z} = -\rho_G v C_p\frac{\partial T_G}{\partial z} + \lambda_G\frac{\partial^2 T_G}{\partial z^2} - S_V K_T(T_G - T_S) \tag{3}$$

$$\text{Solid EB:}\quad \frac{1-\varepsilon}{\varepsilon}\rho_S C_{p,S}\frac{\partial T_S}{\partial t} = \frac{1-\varepsilon}{\varepsilon} f\frac{\partial}{\partial z}\left(\lambda_S\frac{\partial T_S}{\partial z}\right) + S_V K_T(T_G - T_S) - S_{V,C}\left(\sum_{k=1}^{\text{Nsp}} h_k \dot{S}_k\right) - S_V\sigma\left(T_S^4 - \frac{K}{2}\int_{-\infty}^{+\infty} T_S^4(z+z^*)e^{-K|z^*|}dz^*\right) \tag{4}$$

The ideal gas law completes the model. All thermodynamic and transport properties of the gas were estimated as functions of local temperature and composition. The Bulk MB contains the terms of accumulation, convection, axial diffusion and flux from the bulk to the surface for the molecular species H_2, O_2, H_2O, CH_4, CO, CO_2 and Ar. In the BL MB, the accumulation term equals the flux from the bulk to the surface plus species production or consumption at the catalyst surface. The Bulk EB is analogous to the Bulk MB, containing accumulation, convection, axial conduction and the heat flux from the bulk to the solid. The contributions of gas heat conduction and diffusion have to be included in the model because the Pe_M and Pe_T are close to unity. In the solid EB, convection cannot exist, and the accumulation and conduction terms have to be written on a solid volume basis. For this reason, it must be multiplied by $(1-\varepsilon)/\varepsilon$, i.e. the solid to void volume fractions. Since the solid structure of the monolith has a discontinuous nature, the heat conduction in the axial direction finds high resistance (taken into account through a tortuosity factor). Heat transfer by radiation from one pore face to the others (while the amount of radiation absorbed by the gas is neglected) becomes very important at high temperatures, as the emitted power increases with the 4th power of the temperature. The integral term represents the total amount of radiant energy absorbed by the foam support, considered as a black body, in both directions, with an extinction coefficient accounting for light penetration. The equation system comprises 16 partial differential equations first-order with respect to time and second order with respect to axial coordinate, with the exception of the BL MBs, which only have the time derivative.

3.1.1. Boundary conditions

3.1.1.1. Front heat shield (FHS) inlet (z = 0). The gas temperature and composition are those in the feed. These result in Nsp + 1 Dirichlet boundary conditions:

$$\boldsymbol{Y}_G = \boldsymbol{Y}_{G,feed} \text{ and } T_G = T_{G,feed}$$

Due to the presence of a heat shield and the relatively low temperatures, no radiation leaves the reactor. One additional Neumann boundary condition applies:

$$\left.\frac{\partial T_S}{\partial z}\right|_{z=0} = 0$$

3.1.1.2. Back heat shield (BHS) outlet (z = 0.03 m). At the exit, we neglect radiation leaving the BHS, as well, obtaining a zero gradient condition for the solid temperature profile. This assumption is justified because the heat losses by radiation at the BHS are less than 5% of the total amount released by the reaction, estimated from the global energy balance on the experimental data. Furthermore, since gas and solid temperatures have approached each other at the end of the BHS, the gas temperature gradient is negligible and there is no conduction in the gas at the exit. The gas diffusivity is also set to zero at the exit because no concentration gradients are expected one centimeter downstream the catalyst. Therefore, Nsp + 2 Neumann boundary conditions apply at the exit of the BHS.

$$\left.\frac{\partial \boldsymbol{Y}_G}{\partial z}\right|_{z=0.03\text{m}} = 0,\ \left.\frac{\partial T_G}{\partial z}\right|_{z=0.03\text{m}} \text{ and } \left.\frac{\partial T_S}{\partial z}\right|_{z=0.03\text{m}} = 0$$

3.1.1.3. Initial guess (t = 0). The calculations reflect the same start-up procedure followed in the laboratory experiments. Starting from a cold reactor with flowing feed gas, the central catalytic monolith is heated up to the light-off temperature of the catalyst with an external heat source added in the right-hand member of Eq. (4). After reaction light-off, the heater is switched off and the reactor operates autothermally approaching steady state. A change in the operation conditions, for example a switch from one composition to another or to a new flowrate, is simulated such that the previous steady state solution is used as a starting point from which the new steady state is approached.

3.1.2. Equations' parameters

As in Ref. [16], the solid component of the foam was considered polycrystalline alpha-alumina, whose intrinsic thermal conductivity was taken as a function of temperature [34].

$$\lambda_S\ (\text{J S}^{-1}\ \text{m}^{-1}\ \text{K}^{-1}) = 103.7 - 0.3782\cdot T + 6.843\cdot 10^{-4}\cdot T^2 - 6.986\cdot 10^{-7}\cdot T^3 + 4.058\cdot 10^{-10}\cdot T^4 - 1.245\cdot 10^{-13}\cdot T^5 + 1.564\cdot 10^{-17}\cdot T^6$$

Pore diameter, porosity and the value of the extinction coefficient were measured with image analysis [23]. The tortuosity factor was taken from Ref. [35]. Transport coefficient correlations were obtained for an 80 ppi foam through dedicated experiments, which are described in detail in Ref. [23].

$$Sh' = 0.0483\text{Re}'^{0.753}\text{Sc}^{1/3}$$

All numbers marked with a prime indicate that are based on the total bed volume.

3.1.3. Microkinetic model

The microkinetic model for CH_4 oxidation on Rh was initially developed by Schmidt et al. [4] and subsequently improved by others [5] to a final 38-step surface mechanism, involving seven gas species and 12 surface species (Table 1). It contains adsorption and desorption reactions, as well as the proper surface reactions.

In general, the kinetic constants are provided either in the modified Arrhenius expression or as sticking coefficients, and in both cases it can be function of the surface coverage [36], and the reaction order can be different from the stoichiometric coefficient. In the mechanism used, Adsorption Reactions 1–6 are defined

Table 1
Surface reaction mechanism for methane CPO on Rh [29].

	A (cm, mol, s)	E_a (kJ mol^{-1})
1. Adsorption		
$H_2 + Rh_{(s)} + Rh_{(s)} \rightarrow H_{(s)} + H_{(s)}$	1.000×10^{-02}	s.c.[a]
$O_2 + Rh_{(s)} + Rh_{(s)} \rightarrow O_{(s)} + O_{(s)}$	1.000×10^{-02}	s.c.[a]
$CH_4 + Rh_{(s)} \rightarrow CH_{4(s)}$	8.000×10^{-03}	s.c.[a]
$H_2O + Rh_{(s)} \rightarrow H_2O_{(s)}$	1.000×10^{-01}	s.c.[a]
$CO_2 + Rh_{(s)} \rightarrow CO_{2(s)}$	1.000×10^{-05}	s.c.[a]
$CO + Rh_{(s)} \rightarrow CO_{(s)}$	5.000×10^{-01}	s.c.[a]
2. Desorption		
$H_{(s)} + H_{(s)} \rightarrow Rh_{(s)} + Rh_{(s)} + H_2$	$3.000 \times 10^{+21}$	77.8
$O_{(s)} + O_{(s)} \rightarrow Rh_{(s)} + Rh_{(s)} + O_2$	$1.300 \times 10^{+22}$	$355.2 - 280\theta_{O(s)}$
$H_2O_{(s)} \rightarrow H_2O + Rh_{(s)}$	$3.000 \times 10^{+13}$	45.0
$CO_{(s)} \rightarrow CO + Rh_{(s)}$	$3.500 \times 10^{+13}$	$133.4 - 15\theta_{CO(s)}$
$CO_{2(s)} \rightarrow CO_2 + Rh_{(s)}$	$1.000 \times 10^{+13}$	21.7
$CH_{4(s)} \rightarrow CH_4 + Rh_{(s)}$	$1.000 \times 10^{+13}$	25.1
3. Surface reactions		
$H_{(s)} + O_{(s)} \rightarrow OH_{(s)} + Rh_{(s)}$	$5.000 \times 10^{+22}$	83.7
$OH_{(s)} + Rh_{(s)} \rightarrow H_{(s)} + O_{(s)}$	$3.000 \times 10^{+20}$	37.7
$H_{(s)} + OH_{(s)} \rightarrow H_2O_{(s)} + Rh_{(s)}$	$3.000 \times 10^{+20}$	33.5
$H_2O_{(s)} + Rh_{(s)} \rightarrow H_{(s)} + OH_{(s)}$	$5.000 \times 10^{+22}$	104.7
$OH_{(s)} + OH_{(s)} \rightarrow H_2O_{(s)} + O_{(s)}$	$3.000 \times 10^{+21}$	100.8
$H_2O_{(s)} + O_{(s)} \rightarrow OH_{(s)} + OH_{(s)}$	$3.000 \times 10^{+21}$	171.8
$C_{(s)} + O_{(s)} \rightarrow CO_{(s)} + Rh_{(s)}$	$3.000 \times 10^{+22}$	97.9
$CO_{(s)} + Rh_{(s)} \rightarrow C_{(s)} + O_{(s)}$	$2.500 \times 10^{+21}$	169.0
$CO_{(s)} + O_{(s)} \rightarrow CO_{2(s)} + Rh_{(s)}$	$1.400 \times 10^{+20}$	121.6
$CO_{2(s)} + Rh_{(s)} \rightarrow CO_{(s)} + O_{(s)}$	$3.000 \times 10^{+21}$	115.3
$CH_{4(s)} + Rh_{(s)} \rightarrow CH_{3(s)} + H_{(s)}$	$3.700 \times 10^{+21}$	61.0
$CH_{3(s)} + H_{(s)} \rightarrow CH_{4(s)} + Rh_{(s)}$	$3.700 \times 10^{+21}$	51.0
$CH_{3(s)} + Rh_{(s)} \rightarrow CH_{2(s)} + H_{(s)}$	$3.700 \times 10^{+24}$	103.0
$CH_{2(s)} + H_{(s)} \rightarrow CH_{3(s)} + Rh_{(s)}$	$3.700 \times 10^{+21}$	44.0
$CH_{2(s)} + Rh_{(s)} \rightarrow CH_{(s)} + H_{(s)}$	$3.700 \times 10^{+24}$	100.0
$CH_{(s)} + H_{(s)} \rightarrow CH_{2(s)} + Rh_{(s)}$	$3.700 \times 10^{+21}$	68.0
$CH_{(s)} + Rh_{(s)} \rightarrow C_{(s)} + H_{(s)}$	$3.700 \times 10^{+21}$	21.0
$C_{(s)} + H_{(s)} \rightarrow CH_{(s)} + Rh_{(s)}$	$3.700 \times 10^{+21}$	172.8
$CH_{4(s)} + O_{(s)} \rightarrow CH_{3(s)} + OH_{(s)}$	$1.700 \times 10^{+24}$	80.3
$CH_{3(s)} + OH_{(s)} \rightarrow CH_{4(s)} + O_{(s)}$	$3.700 \times 10^{+21}$	24.3
$CH_{3(s)} + O_{(s)} \rightarrow CH_{2(s)} + OH_{(s)}$	$3.700 \times 10^{+24}$	120.3
$CH_{2(s)} + OH_{(s)} \rightarrow CH_{3(s)} + O_{(s)}$	$3.700 \times 10^{+21}$	15.1
$CH_{2(s)} + O_{(s)} \rightarrow CH_{(s)} + OH_{(s)}$	$3.700 \times 10^{+24}$	158.4
$CH_{(s)} + OH_{(s)} \rightarrow CH_{2(s)} + O_{(s)}$	$3.700 \times 10^{+21}$	36.8
$CH_{(s)} + O_{(s)} \rightarrow C_{(s)} + OH_{(s)}$	$3.700 \times 10^{+21}$	30.1
$C_{(s)} + OH_{(s)} \rightarrow CH_{(s)} + O_{(s)}$	$3.700 \times 10^{+21}$	145.5

[a] Value of sticking coefficient. Surface site density: $\Gamma = 2.72 \times 10^{-9}$ mol cm^{-2}.

through a sticking coefficient and in O_2 and CO Desorption Reactions 8, 10, the kinetic constant is modified by the coverages concentration of the oxygen surface species, $O_{(s)}$. Because of all these features, the kinetics is handled by an interpreter, which reads the mechanism written in standard CHEMKIN format and returns the calculated production rate and the heats of reaction at local temperature and composition. Cantera [37] was chosen as interpreter because of its Matlab [38] interface, which makes the species production rates as well as the thermodynamic and transport properties available to the main program. Thermodynamic data were taken from the GRImech3.0 database [39].

3.2. Modeling results for reference C/O = 1 and 5 slpm flowrate

The modeling results for the reference case at C/O = 1 and F = 5 slpm are reported in Fig. 5, where they are compared with the experimental species profiles. Methane conversion will be used in the following, being a more concise representation, to compare modeled and experimental data at different conditions, while H_2 and CO selectivities will be calculated to analyze the species distribution differences between experiments and model.

The model follows the experimental profiles very closely, with three exceptions. Right at the entrance of the catalyst, within the first 0.5 mm, the experimental reactant conversion is significantly

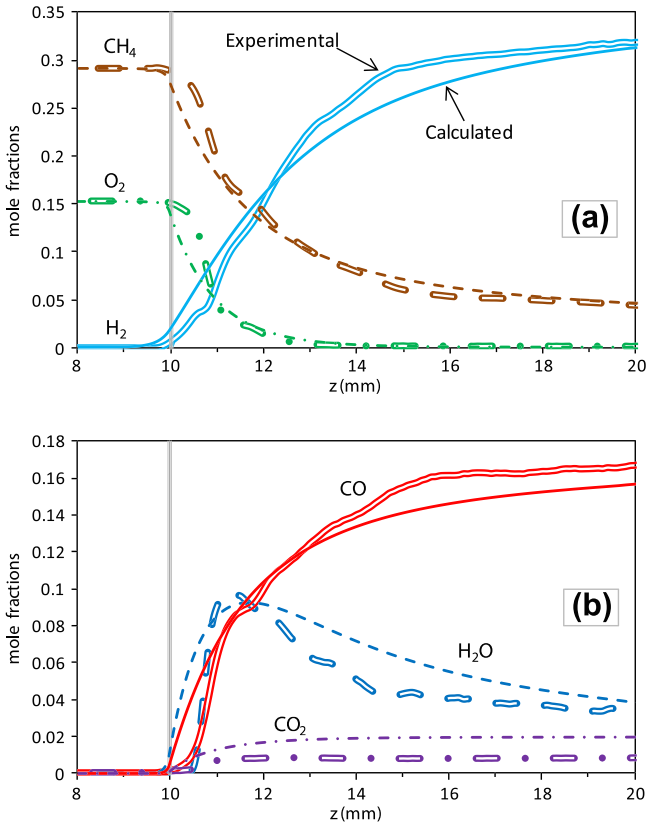

Fig. 5. Experimental (double line) vs. calculated (single line) species profiles at total inlet flowrate F = 5 slpm and stoichiometry C/O = 1.0. CH_4, O_2 and H_2 mole fractions (panel a), CO, H_2O and CO_2 (panel b). The catalyst section falls between 10 mm and 20 mm.

underestimated by the model. This lack of predictions remains with different flowrates, as shown later, and, together with the absence of this trend in data sets obtained with other catalyst supports [6,22], it reinforces the idea that this feature might be due to some physical irregularity of the support, like a blocked pore. Also, the bump at 12 mm (2 mm inside the catalyst) might be of similar origin. On the other side, a zone of higher conversion exists between 14 mm and 17 mm. Also, this feature does not move with increasing the flowrate and is therefore most likely linked to the geometry of the support.

Furthermore, the evolution of the products is well captured by the model apart from an underestimation of CO production in favor of CO_2. The most severe disagreement between experiment and model is a lower predicted surface temperature, which is a possible cause of the lower selectivity to CO, as discussed in the introduction.

3.3. Modeling different C/O ratios

Data reported in Fig. 2 were modeled, and results are showed in Fig. 6. Most of the features in the experimental profiles are reproduced by the model (Fig. 6a). The three O_2 profiles overlap shortly after the entrance of the catalyst and decline then with the same rate. CH_4 reacts more vigorously in the leaner mixture (see also Fig. 7), where the surface temperature is highest. Hydrogen production is very similar in the C/O = 0.8 and 1 cases, for which supposedly its production is limited mostly by the transfer phenomena (availability of methane at the catalytic surface), while it is tangibly lower for the C/O = 1.3, probably in mixed mass transfer–kinetic regime for CH_4, mimicking the experimental trend.

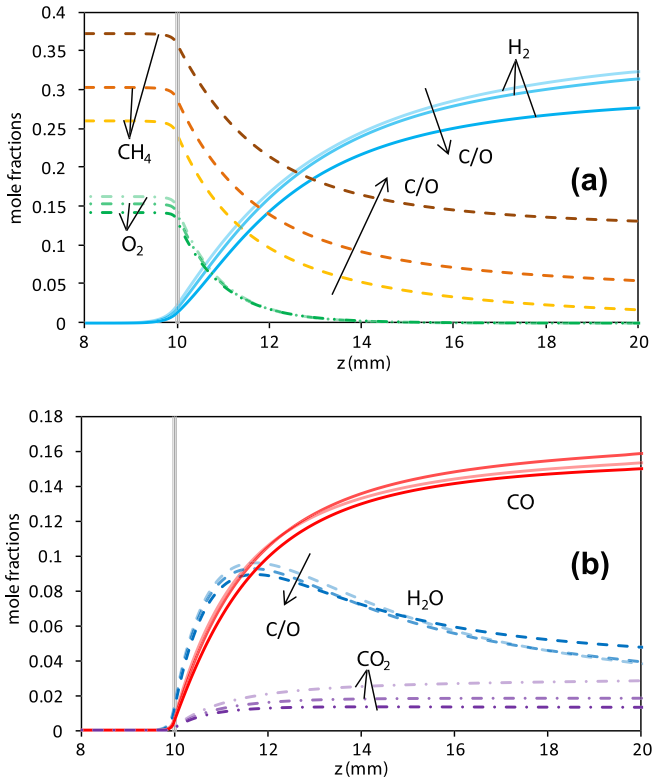

Fig. 6. Calculated species profiles at total inlet flowrate $F = 5$ slpm and stoichiometry C/O = 0.8, 1.0, 1.3 (lighter to darker color). CH_4, O_2 and H_2 mole fractions (panel a), CO, H_2O and CO_2 (panel b). The catalyst section falls between 10 mm and 20 mm.

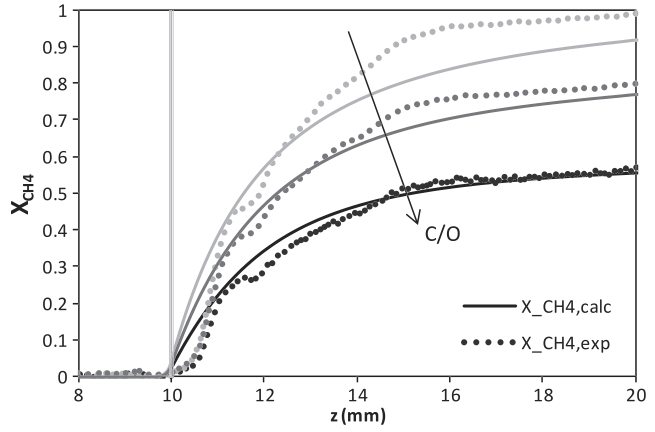

Fig. 7. Experimental vs. calculated profiles of methane conversion at total inlet flowrate $F = 5$ slpm and stoichiometry C/O = 0.8, 1.0, 1.3 (lighter to darker gray). The catalyst section falls between 10 mm and 20 mm.

Some discrepancies are observed in Fig. 6b, showing the modeled species profiles for H_2O, CO and CO_2. The corresponding experimental profiles are shown in Fig. 2b. H_2O profiles behave as in the experiments. The peak water mole fraction is higher for the low C/O because more O_2 is available for total oxidation (R1). Further downstream, the higher temperatures in the C/O = 0.8 and 1.0 case allow a faster water consumption by steam reforming (R4). Given the lower temperatures prevailing in the C/O = 1.3 case, steam reforming is slower and more water remains in the effluent stream. The CO data show the most interesting features. Unlike the experimental profiles, the calculated curves are very similar for all the three C/O ratios investigated. Therefore, the model clearly implements two different routes to H_2 and CO, independent of one another. The CO_2 curves are overestimated at the lower C/Os. Interestingly, similarly to what happens in the experiments, the CO_2 reaches inside the catalyst a plateau for C/O = 1.3 and 1, but keeps increasing for the C/O = 0.8. This is not due to some residual presence of O_2 in the gas phase, as discussed later, since the O_2 left is even lower than in the other cases, because of a lower inlet concentration but mostly due to the higher temperatures ($T_S > 800$ °C).

A more informative and concise way to compare experimental and calculated species profiles at different C/O ratios is by plotting methane conversion instead of mole fractions (Fig. 7). Aside from the entrance region, the agreement is excellent for C/O = 1.3. The oxidation zone is well described by all calculated profiles, whereas in the reforming zone some discrepancies remain at lower C/O. A similar mismatch is observed between the experimental and calculated temperature profiles at C/O = 0.8 (Fig. 8). Even though the solid temperature maximum is well described by the model, the decrease of the surface temperature in the model due to chemical cooling by steam reforming is predicted much slower than observed experimentally. Obviously, the transfer phenomena (convection, axial diffusion and bulk-BL mass transfer) in the oxidation zone are well captured by the model, whereas surface kinetics in the steam reforming zone are insufficiently described. A very sensitive parameter, of direct influence on any surface reaction rate, is the active catalytic surface area per unit volume $S_{V,C}$. The effect of this parameter was investigated and is reported in the "Discussion" section.

3.4. Modeling different flowrates

Calculated profiles at different flowrates are shown in Fig. 9. As expected, increasing the flowrate shifts all profiles downstream, but modifies them also in other ways. Diffusion smoothes steep gradients more effectively at low flowrates (low Pe), while it is becoming less important at higher flowrates (high Pe). The effect of diffusion is particularly evident near the catalyst entrance, where there is a rounding of all species profiles, mostly that of H_2. Apart from increasing the Pe numbers for mass and heat, increasing the flowrate enhances heat and mass transfer between the gas and the solid, such that in some region inside the catalyst foam, the overall reaction can change from diffusion limited to a kinetically controlled regime via a mixed regime in between (see "Discussion"). On the other hand, increasing the flowrate lowers the residence time, which in turn leads to a decrease in conversion.

As observed experimentally (cp. to Fig. 4), there is an evident shifting of all profiles, particularly evident in the oxidation zone. Model predicts that methane and oxygen decrease before reaching

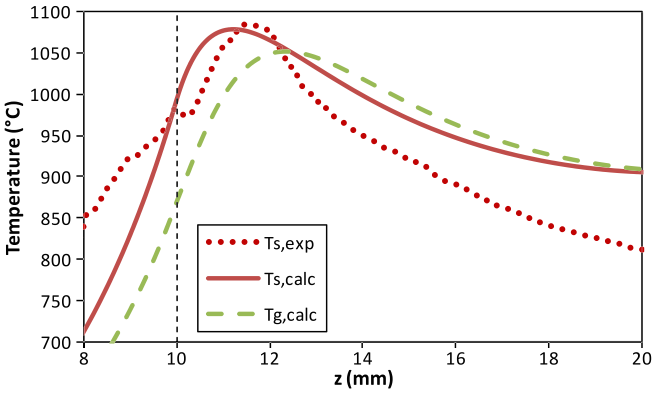

Fig. 8. Calculated temperature profiles (solid: solid, dashed: gas) compared to the experimental pyrometer measurement (dots) at total inlet flowrate $F = 5$ slpm and stoichiometry C/O = 0.8. The catalyst section falls between 10 mm and 20 mm.

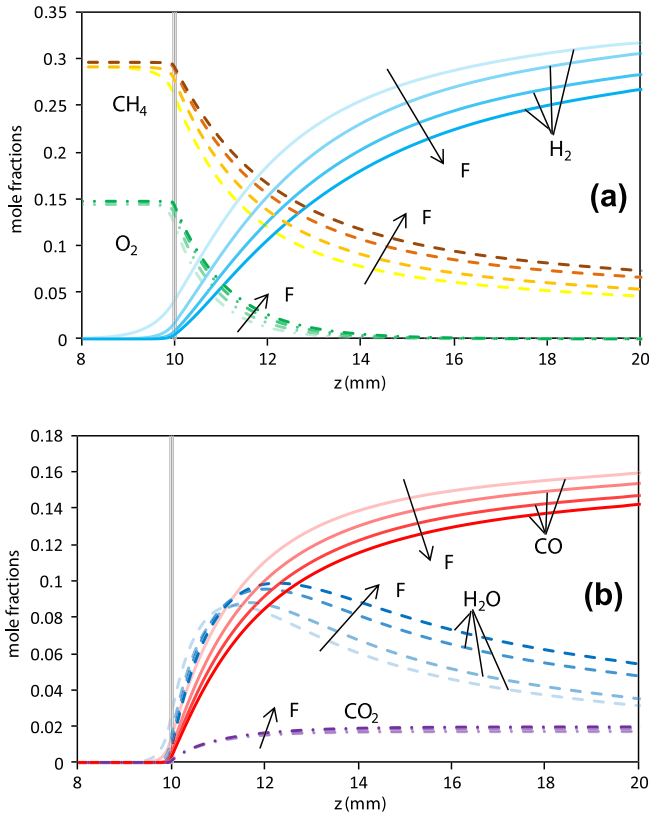

Fig. 9. Calculated species profiles at total inlet flowrates of F = 2.5, 5, 7.5, 10 slpm (lighter to darkercolor) and at C/O = 1.0 stoichiometry. CH_4, O_2 and H_2 mole fractions (panel a), CO, H_2O and CO_2 (panel b). The catalyst section falls between 10 mm and 20 mm.

the catalyst at the lowest flowrate (2.5 slpm), because of forward-diffusion, as measured also, whereas at the highest (10 slpm), both suddenly begin reacting at the catalyst inlet. This diffusion effect separates the profiles already at z = 0.01 mm, which means the reactants reach the catalyst inlet with a different composition depending on the flowrate. Inside the catalyst, increasing the flowrate leads to a shorter contact time and, in consequence, lower methane conversion and lower H_2 and CO yields. The H_2O profiles are also shifted downstream but show a more complicated trend due to a complex interplay of transport and kinetics. Due to an increase in flowrate, the oxidation zone widens, leading to an increase in catalyst temperature (Fig. 10) and of the height of the water peak. At the same time, the higher surface temperature leads to a higher rate of endothermic steam reforming. In the calculated profiles, water production due to oxidation is more pronounced than water consumption due to reforming. Therefore, the model predicts an increase of the water peak with increasing flowrate. In the experiments, the trend of the maxima is opposite. The peak H_2O mole fraction at 2.5 slpm is higher than at 10 slpm, indicating that steam reforming is predicted too slow by the model possibly due to an underestimation of the available catalytic area in the model. It has to be recalled that the oxidation zone is defined as the length of the catalyst where oxygen is present among the gas species, while in the reforming zone, only SR, WGS and DR (R4-6) are possible. But the reforming reactions start already in the oxidation zone, which is proved by the negative H_2O gradient. In fact, oxidation is not affected by the $S_{V,C}$ parameter, because it runs in diffusion regime, while reforming, controlled by the kinetics, is proportional to the active catalytic surface. The discrepancy between model and experiment is most pronounced at the highest flowrate, where mass transfer is enhanced and steam reforming kinetics start influencing the conversion, also in the oxidation zone. As a consequence, a good estimation of the active catalytic surface becomes important also in the oxidation zone, at higher flowrates, because the reactions run in mixed regime. Similar to what is observed in experiments, CO_2 profiles are less strongly affected by the flowrate as CO_2 is only formed in the oxidation zone where transport dominates and kinetics is less important. Once again, the model describes accurately the mass transport phenomena. Nonetheless, it has to be noticed that, similarly to what happens in the reference case, the CO_2 predicted is about twice as much as in the experiments, meaning that there is some factor affecting the carbon selectivity, which is still to be identified but is most likely linked to the chemistry.

In the reforming zone, the curves at different F, which were differentiated already in the oxidation zone, remain separated as they rise with similar slopes. The experimental profiles, on the contrary, have very different behavior in the middle of the catalyst, where the reactivity is much higher for the highest flowrates, so that the four curves approach one another toward the end of the catalyst. The reason for this different behavior is not clear: errors in the kinetics or in the temperature description or underestimated/irregular active area distribution are possible causes of this discrepancy.

Fig. 11 shows a comparison of the experimental and calculated methane conversion profiles. The agreement at 2.5 slpm is remarkable, while at 10 slpm, there is no concordance, either at the inlet

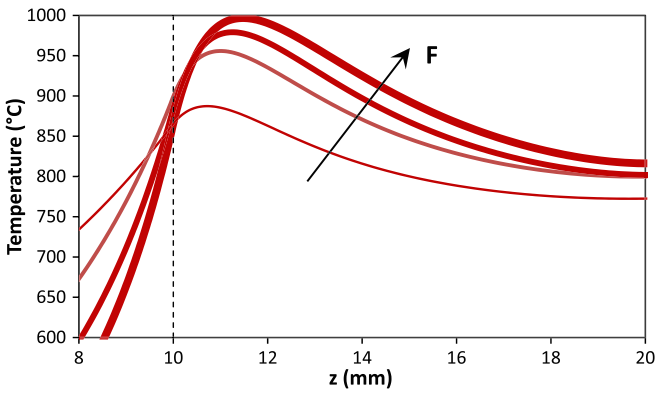

Fig. 10. Calculated solid temperature profiles at total inlet flowrates F = 2.5, 5, 7.5, 10 slpm (thinner to thicker lines) and C/O = 1 stoichiometry. The catalyst section falls between 10 mm and 20 mm.

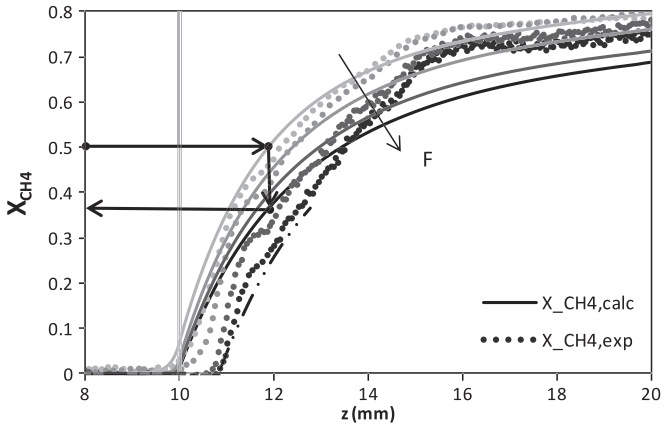

Fig. 11. Experimental vs. calculated profiles of methane conversion at total inlet flowrate F = 2.5, 5, 7.5, 10 slpm (lighter to darker gray) and C/O = 1.0 stoichiometry. The catalyst section falls between 10 mm and 20 mm. The dash-dot-dot line represents the F = 10 slpm curve, shifted downstream.

or at the outlet of the catalyst zone. Nonetheless, the slope of the calculated curve at 10 slpm matches that of the experimental one in the oxidation zone, if it is shifted downstream (dash-dot-dot line), meaning that there is an initial effect in the first millimeter of the catalyst that the model cannot reproduce. The reforming zone is adequately described at low flowrates, but the rate of steam reforming is underestimated at the higher flowrates in the center of the catalyst. In fact, the slopes of the curves are similar in the calculated and experimental profiles, at the end of the catalyst, but they are very different right in the middle, where water concentration and surface temperature are still high.

4. Discussion

The capillary sampling technique is very useful for gathering data in short contact time catalytic partial oxidation processes. The measured species and temperature profiles offer a unique opportunity for interpreting the data with detailed models, recognizing the contribution of physical and chemical phenomena, through the implementation of the more relevant transfer phenomena and the inclusion of a micro kinetic mechanism. Such a comparison allows in a first step the refinement of the model itself in terms of heat transport, mass transport and surface kinetic description and in a second step, after agreement with the experimental profiles is reached, a quantitative assessment of the interplay between transport and chemistry on the one hand and the catalytic reaction pathways on the other hand.

The reliability of the model has once again been confirmed by the comparison with the new experimental data measured at different C/O and flowrates. The model is suitable to reproduce both the qualitative and quantitative behavior of the methane CPO on Rh and can therefore be used for an in-depth analysis of the chemical reaction pathways at the Rh surface. Measurements at different inlet composition and total flowrate provide a further opportunity to discuss the validity and criticisms of the available surface chemistry models.

4.1. Kinetics vs. diffusive regime

A discussion about the dominant regime of reaction has been touched on all through the paper, through qualitative analysis of curve shape, for example looking at the trends with changing flowrate or stoichiometry. The discussion can be extended to include other quantitative arguments with the use of the model.

The reaction regime to which the reagents are subjected in the oxidation zone is of primary interest. In the oxidation zone, the diffusive regime of oxygen is almost unquestionable; however, the behavior of methane is ambiguous and suggests a mixed regime for the highest flowrates. A comparison between the transport coefficient and the kinetic constant is reported in Table 2 to show the relative rates of reaction and transport for O_2 and CH_4. Since reactants do not undergo a single first-order reaction, but a detailed kinetic mechanism, the kinetic constant of the corresponding first-order reaction, called the pseudo-first-order kinetic constant, is calculated as the ratio between the consumption rate of the reactant and its concentration:

$$k_i^* = \frac{-\dot{s}_i}{c_i} \quad i = O_2,\ CH_4$$

The feed concentration was used to calculate the transport properties and the surface reactions. The temperature of 1000 °C = 1273 K was chosen for all the four cases to simplify the comparison, although analogous results (not shown) can be obtained applying the actual surface temperatures, spanning from 1160 K to 1325 K at the surface temperature peaks.

Transport coefficient of CH_4 is about 20% higher than O_2's. They both increase with flowrate, proportionally to $F^{0.75}$, as in the transport correlation adopted in the model. On the other hand, having set a unique temperature value for the four cases, the kinetic constant does not depend on F. k^*_{O2} is about 2.5 times k^*_{CH4}. More interesting are the ratios $k^*_{O2}/K_{C,O2}$ and $k^*_{CH4}/K_{C,CH4}$, which give us an indication about the dominant regime. For O_2, the kinetics is 11 times faster than transport, at F = 2.5 slpm, and still four time faster at 10 slpm. Oxygen reacts in diffusive regime for the whole range of F investigated with the experiments. On the other hand, the same ratio, calculated for CH_4, is about 4 at 2.5 slpm, but is close to 1 at 10 slpm. At the highest flowrates, methane reacts in a mixed regime, controlled both by radial diffusion and chemical reaction.

In an attempt to apply a typical parameter analysis [40] for the oxidation zone operating in diffusive regime for CH_4, the conversion at 10 slpm is estimated from the knowledge of the corresponding conversion at 2.5 slpm assuming pure mass transfer control. The effect of flowrate is investigated, e.g. by evaluating which conversion X_2 the 10 slpm curve should have at a position when the 2.5 slpm curve reaches X_1 = 50% conversion. As shown in Fig. 11, X_1 = 50% is reached at about z^* = 0.012 m. By solving the mass balance without diffusion, at steady state and in mass transfer control (Y_{BL} = 0), the following relation is obtained:

$$\frac{ln\frac{1}{1-X_1}}{ln\frac{1}{1-X_2}} = \frac{\frac{K_{C,1}S_V z^*}{v_1}}{\frac{K_{C,2}S_V z^*}{v_2}}$$

The dependence of K_C on the flowrate is, with our correlations, $K_C \propto v^{0.75}$.

$$X_2 = 1 - \frac{1}{exp\left[ln\left(\frac{1}{1-X_1}\right)\cdot\left(\frac{v_2}{v_1}\right)^{0.75-1}\right]} = 1 - \frac{1}{exp\left[ln(2)\cdot(4)^{-0.25}\right]} = 39\%$$

The actual X_2 is 37%, a little lower than that calculated assuming instantaneous kinetics because it was shown that for a high flowrate, the chemistry slows down the conversion even more than the sole mass transfer resistance. As an aside, this simple calculation confirms that an increase in velocity augments the mass transfer coefficient, but the general consequence is a reduction on conversion, at the same position. As the good agreement shows, conversion in the oxidation zone is governed mostly by mass transfer. Nonetheless, as the flow increases, mass transfer becomes more efficient, kinetics can discriminate the results, thus the chemistry model is progressively more important.

4.2. Hydrogen reaction path

The reaction path that leads to H_2 in methane CPO has been a subject of a heated debate in the literature. In the direct path, methane and oxygen, once adsorbed on the surface, produce CO and H_2 straightaway, without any intermediate desorption/adsorption of any other species. In the indirect path, methane participates in total oxidation (TO) reaction (R1), leading to CO_2 and H_2O, which

Table 2
Transport coefficient and pseudo-first-order kinetic constant of O_2 and CH_4 at the different flowrates and 1000 °C. The ratio between the kinetic constant and the transport coefficient is reported as well.

F (slpm)	2.5	5	7.5	10
$K_{C,O2}$ (m s^{-1})	0.280	0.468	0.638	0.795
$K_{C,CH4}$ (m s^{-1})	0.333	0.556	0.758	0.946
k^*_{O2} (m s^{-1})		3.2		
k^*_{CH4} (m s^{-1})		1.3		
$k^*_{O2}/K_{C,O2}$	11.4	6.48	5.01	4.03
$k_{CH4}/K_{C,CH4}$	3.90	2.34	1.72	1.37

leave the surface, and only after a second adsorption step, CO_2 and H_2O react with CH_4 in SR (R4), WGS (R5) and DR (R6) to generate CO and H_2. Some authors suggested a direct H_2 formation path mostly based on results from transient experiments [41]. Other experiments in which product species were added to the feed [42] suggested an indirect path. As shown recently by the authors [14], the experimental measurements might be misleading. Measured gas product compositions refer to the composition of the bulk gas phase, while the gas composition in the boundary layer, i.e. the immediate vicinity of the catalyst surface, might be totally different and contain a substantial water concentration already at the entrance of the catalyst. From experimental observation, it is rather difficult to discriminate between the two pathways, because surface hydrogen atoms $H_{(s)}$ can either produce H_2 ($R2H_2$: $H_{(s)} = ½\ H_2 + \bullet$) or participate in the reactions: $R2OH_{(s)}$: $H_{(s)} + O_{(s)} = OH_{(s)} + \bullet$ or $R2H_2O_{(s)}$: $H_{(s)} + OH_{(s)} = H_2O_{(s)} + \bullet$. Fig. 12 displays results for the reference case C/O = 1.0 and 5 slpm flowrate. In the oxidation zone, the routes $R2OH_{(s)}$ and $R2H_2O_{(s)}$ are about two and three times higher than $R2H_2$, respectively, but $H_{(s)}$ recombination ($R2H_2$) increases, soon ($z > 0.11$ m) prevailing over its consumption reactions ($R2OH_{(s)}$ and $R2H_2O_{(s)}$). In the steam reforming zone, $R2H_2$ remains positive, while $R2OH_{(s)}$ and $R2H_2O_{(s)}$ become negative, because H_2O re-adsorbs on the surface and re-dissociates into $H_{(s)}$ and $O_{(s)}$.

Veser [33] used the same mechanism, in an earlier formulation [4], to evaluate the total amount of H_2 produced via the direct or the indirect path. Using an ideal PFR reactor, with no axial diffusion and infinite diffusivity in the radial direction, he found that the indirect path contributes at most 25% to the total H_2 produced, consistent with the 30% predicted by our model. From this result, he concludes that the main route to H_2 is through a direct path.

According to the production rates of H_2 and H_2O (Fig. 13a), H_2O is preferably produced at the catalyst entrance, but its net formation rate $\dot{S}H_2O$ decreases rapidly and becomes negative at the end of the oxidation zone. H_2 production rate, $\dot{S}_{H_2}$, shows exactly the same trend as $R2H_2$, only the absolute value is doubled. Being the $R2H_{(s)}$: $½\ H_2 + \bullet = H_{(s)}$ the inverse of $R2H_2$ and the only other reaction involving molecular H_2, $\dot{S}_{H2} = 2 \cdot R2H_2 - 2 \cdot R2H_{(S)} \approx 2 \cdot R2H_2$, meaning that the rate of adsorption of H_2 to $H_{(s)}$ is negligible. Even though this analysis is useful for studying the H_2 selectivity, it is misleading in terms of understanding the H_2 formation path. This is due to the fact that a positive production rate of water only means that water production via TO (R1) (or even via H_2 combustion [43]) is greater than its consumption via SR (R4). To study the methane CPO (R2) reaction path without influence of other

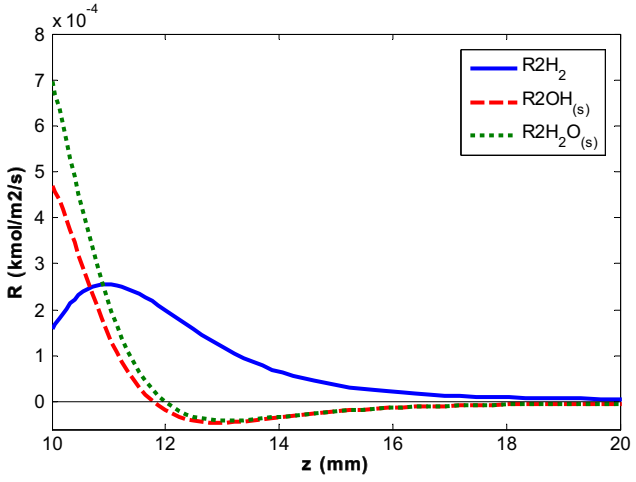

Fig. 12. Reactions involving the surface hydrogen atoms $H_{(s)}$ in the catalytic foam.

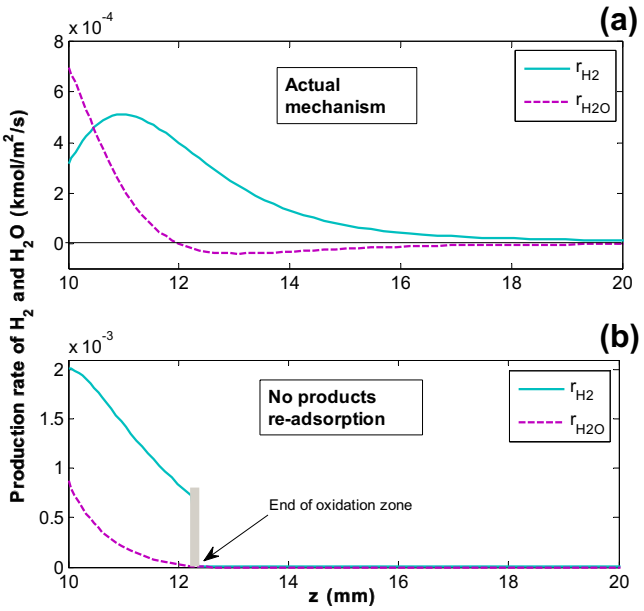

Fig. 13. Production rates of H_2 and H_2O in the catalytic foam. Results using the actual mechanism (panel a) and if product re-adsorption is artificially inhibited (panel b). Vertical scale is different in the two panels.

reactions, adsorption of products was inhibited, i.e. canceling reactions 1, 4, 5, 6 from mechanism showed in Table 1, allowing only adsorption of reactants, i.e. reactions 2, 3. The results are displayed in Fig. 13b. Under the superimposed restrictions in the mechanism, reactions are possible only in the oxidation zone, because after the oxygen is consumed, no other species can adsorb and react on the surface. It is very interesting to note that the water production rate is only slightly higher with inhibited product re-adsorption, simply because it is not involved in any other reactions, e.g. SR: its production rate is limited by the availability of O_2 on the surface. However, most remarkably, H_2 production is nearly three times faster, probably because the surface coverage is different without product re-adsorption and this circumstance favors H_2 production, as well as CO production (not shown). More importantly, since H_2O cannot adsorb back on the surface, all the H_2 produced comes from a direct route. The above results suggest the coexistence of both reaction paths and that H_2 can be a primary product already at the entrance of the catalyst, even with a great presence of O_2.

4.3. Coverages and selectivity trends at different C/O and flowrate

For all investigated C/O ratios, calculated surface coverages of the main surface species are shown in Fig. 14. As expected, in the mass transfer limited oxidation zone, the majority of the Rh sites are free. At the higher C/O ratio, due to the relatively higher amount of carbon atoms in the reactants, the $CO_{(s)}$ and $C_{(s)}$ increase. There is a lower production of CO_2, which causes a smaller heat release. The lower temperature slows down the desorption reaction, which also explains the diminished free surface sites. The general trend of a decreasing fraction of free rhodium sites with increasing C/O is also in line with a gradual transition from a purely mass transfer limited regime in the oxidation zone to a partly kinetically controlled regime, since the site is free when the reaction + desorption occurring on it is much faster than the feeding rate from the gas phase. The $O_{(s)}$ is consumed more rapidly as the gas phase partial pressure of O_2 in the oxidation zone decreases with increasing C/O. The $H_{(s)}$ coverage decreases at higher C/O ratio.

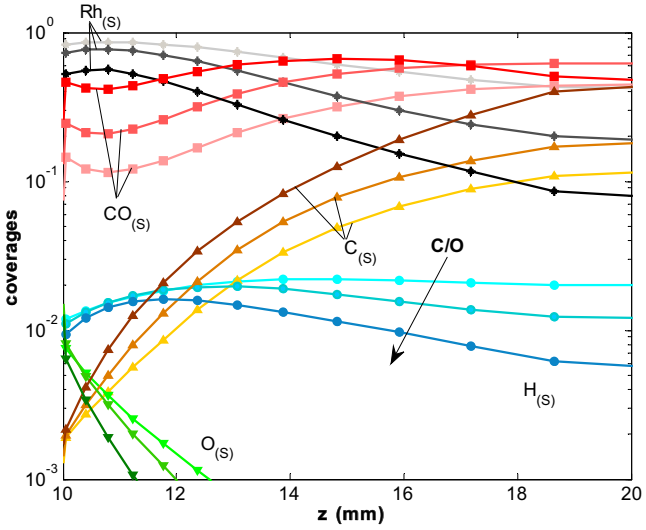

Fig. 14. Main fractional surface coverages in the catalytic foam at total inlet flowrate F = 5 slpm and stoichiometry C/O = 0.8, 1.0, 1.3 (lighter to darker color).

The calculated integral selectivities, defined locally as $S_{H2} = c_{H2}/(c_{H2} + c_{H2O})$ and $S_{CO} = c_{CO}/(c_{CO} + c_{CO2})$, depend differently on the C/O ratio (Fig. 15). Furthermore, the model predicts different trends than are observed experimentally. For the leanest stoichiometry (C/O = 0.8), where surface temperatures are highest, the model predicts the lowest selectivity to CO (S_{CO}), exactly opposite to the experiments where S_{CO} is highest for C/O = 0.8. The consequence of an underestimation of S_{CO} is of course an overestimation of S_{CO2}, as guessed from the observation of the concentration profiles. The S_{H2} curves from the model almost overlap in the steam reforming zone in the case of C/O = 0.8 and C/O = 1, whereas it is lower for C/O = 1.3. This time the model follows the experimental trend, even though the model underpredicts H_2 production in the reforming zone and thus its selectivity. There is a minimum in the H_2 selectivity, near the entrance. This behavior apparently confirms the presence of some H_2 combustion. In reality, it is only an artifact due to the combination of axial and radial diffusion: the bulk gas composition is different from that in the boundary layer and in particular H_2 diffuses much faster than H_2O, determining the presence of H_2 in the gas upstream the catalyst entrance, where hydrogen selectivity is already high even though the reaction has not started. In fact, the same figure (not shown), drawn with the boundary layer compositions, would give a monotonic trend for S_{H2}. The fact that the experimental data presents the same minimum is due to the same effect of diffusion. Furthermore, the selectivity to H_2 increases in the axial direction, with methane conversion, as a combined result of CPO (R2) and SR (R4).

Thermodynamic equilibrium, evaluated at the C/O = 0.8 stoichiometry, confirms that the experimental methane conversion approaches the equilibrium value, which is close to unity (Table 3). The model reaches only 94%. The exit temperatures reflect these results as well. Since endothermic steam reforming SR (R4) does not reach equilibrium, the experimental temperature at the end of the catalyst is slightly higher (only 2 °C) than the thermodynamic adiabatic temperature. On the other hand, the calculated exit methane conversion is 5.5% lower than equilibrium leading to a 100 °C higher exit temperature than equilibrium. Hydrogen selectivity is the same in both the experiment and the model and only 1.5% lower than equilibrium. The calculated exit CO selectivity is significantly lower than equilibrium, while in the experimental data, it is even higher. This is a desired behavior and typical for Rh as catalyst, which has the ability to increase S_{CO} above the equilibrium value. Nonetheless, the high temperatures (T_S > 800 °C) reached by the catalyst enhance the rate of WGS (R5), increasing S_{H2} and reducing S_{CO}, which passes through a maximum at about 2/3 of the catalyst and then decreases toward the equilibrium value (Fig. 16), calculated at constant pressure and enthalpy, starting from the feedstock composition at 100 °C. This behavior is reflected by the observed rise of the CO_2 profile, both experimental and calculated, noticed only at the high surface temperatures in this particular experiment. Rhodium is confirmed, both from experimental and numerical evidences, in its role of enhancing the syngas selec-

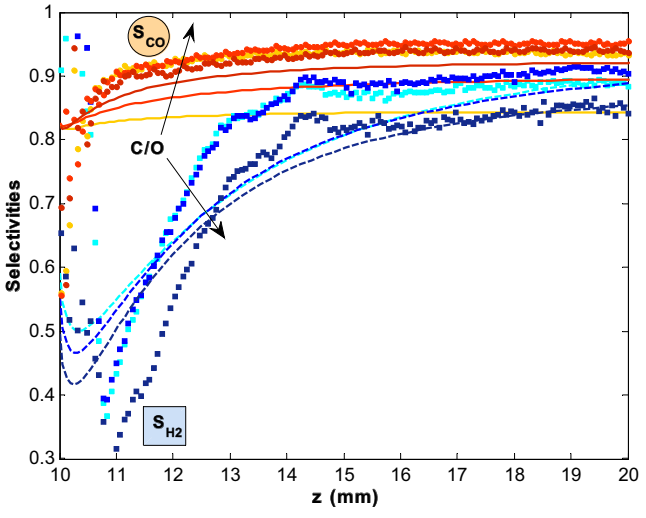

Fig. 15. Syngas selectivity in the catalytic foam at total inlet flowrate F = 5 slpm and stoichiometry C/O = 0.8, 1.0, 1.3 (lighter to darkercolor). Solid lines and circles correspond to numerical and experimental S_{CO}, respectively. Dashed lines and squares relate to S_{H2}.

Table 3
Conversion and selectivities at the exit of the catalyst section for the C/O = 0.8 stoichiometry (T_{inlet} = 100 °C). Thermodynamic equilibrium (iso-H and iso-P) vs. experimental and calculated data.

	Equilibrium	Experimental	Model
X_{CH4} (%)	99.5	99	94
T (°C)	810	812	910
S_{H2} (%)	91.5	89	89
S_{CO} (%)	91	94	84

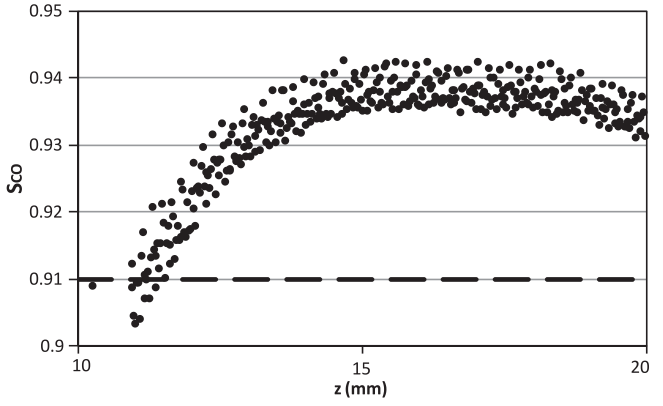

Fig. 16. CO experimental selectivity (dots) at total inlet flowrate F = 5 slpm and stoichiometry C/O = 0.8, compared with the adiabatic equilibrium value (dashed line) in the catalytic foam. The real sampling rate is used in plotting the experimental data.

tivity, depleting the production of CO_2 in favor of the CO, i.e. not catalyzing the WGS reaction (R5). On the other hand, given the higher surface temperature in the C/O = 0.8 test, some shifting of the product composition toward equilibrium is likely to occur. The WGS reaction, which does not appear to reach equilibrium for C/O = 1.3 and 1, is kinetically favored by the higher temperature and occurs along the entire catalyst, changing the composition accordingly to the equilibrium.

Fig. 17 shows how the coverages of the main surface species change with flowrate. The resulting curves are the result of a complex interplay between increased surface temperature, increased mass and heat transfer in radial direction, decreased contact time and decreased relevance of axial diffusion. Contrary to what happens increasing C/O, at higher *F* surface oxygen atoms $O_{(s)}$ remain on the Rh surface for longer, simply because gas phase oxygen is now consumed over a longer section of catalyst than at low flowrates. In general, all profiles are shifted downstream, also with modifications in their shapes. $CO_{(s)}$ decreases and forms a minimum in the oxidation zone; this is more pronounced at higher *F*. $C_{(s)}$ is simply translated downstream. $H_{(s)}$ shows an inversion, along the catalyst: at the catalyst entrance its coverage decreases with increasing *F*, while at the exit, it shows the opposite trend. Rh-free sites increase at higher *F*, confirming that when rising the flowrate, the process becomes increasingly kinetically controlled.

In terms of selectivities, increasing F does not have the same effect as decreasing C/O (Fig. 18). Both S_{CO} and S_{H2} decrease with flowrate, which also happens in the experiments. S_{CO} is generally under predicted by the model, while S_{H2} shows a better general agreement with the experimental selectivity. The minima in the S_{H2} curves are present both in the experimental and model curves, whereas the minima in the model are at a fixed axial coordinate, the experimental minimum shifts downstream with increasing *F*. At all flowrates, the experimental S_{CO} grows monotonically and reaches values higher than equilibrium at the catalyst exit, e.g. at $F = 10$ slpm, $S_{CO,exp} = 94.5\% > S_{CO,equil} = 91\%$. The calculated value reaches only $S_{CO,model} = 88\%$. Opposite to the behavior at C/O = 0.8, there is no continuous production of CO_2 along the entire catalyst as the surface temperature is 100 °C lower (cp. Figs. 3 and 10).

In summary, according to the model, increasing C/O or decreasing *F* (i.e. increasing the residence time) results in a higher $CO_{(s)}$ coverage on the surface. In terms of selectivities, increasing C/O increases S_{CO} but decreases S_{H2}, whereas both S_{CO} and S_{H2} increase with decreasing *F*. The first effect is mostly due to the WGS equilibrium, since a lower C/O implies higher *T* and the equilibrium of the exothermic WGS is shifted toward the reactants CO and H_2O. The second effect upon lowering *F* is probably due to the comparably slow rate of steam reforming, which has at low flowrates more time to proceed than at high flowrates.

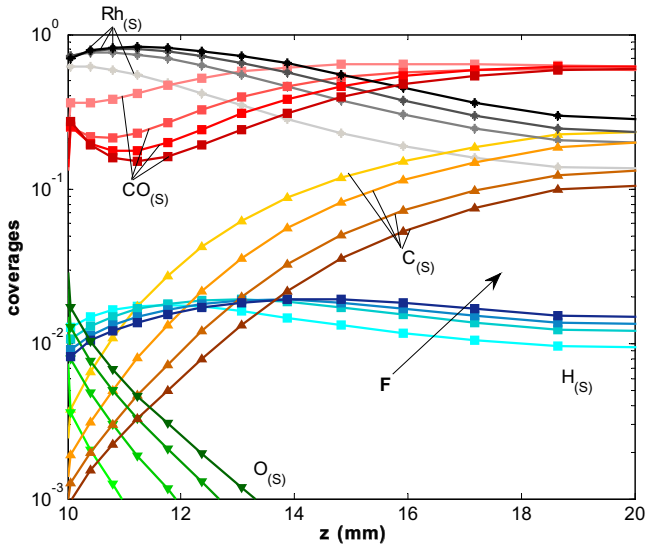

Fig. 17. Main fractional surface coverages in the catalytic foam at total inlet flowrate *F* = 2.5, 5, 7.5, 10 slpm (lighter to darker color) and stoichiometry C/O = 1.0.

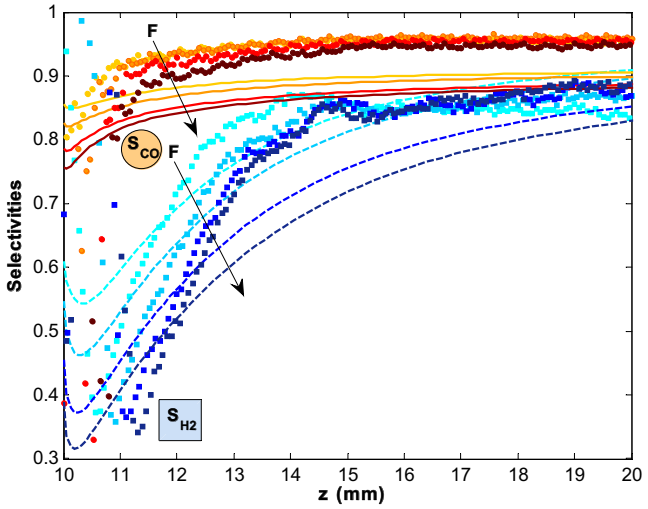

Fig. 18. Syngas selectivity in the catalytic foam at total inlet flowrate *F* = 2.5, 5, 7.5, 10 slpm (lighter to darker color) and C/O = 1.0 stoichiometry. Solid lines and filled circles correspond to numerical and experimental S_{CO}, respectively. Dashed lines and filled squares relate to S_{H2}.

4.4. Sensitivity analysis to the active catalytic surface

Specific surface of the catalyst is key information. We measured the pore size through image analysis of the foam, as described in [23]. From the pore size, the surface of the support was determined and the surface-to-volume ratio calculated as $S_V = 8000\ m^{-1}$. Specific surface is required in the model equations to calculate the volumetric contribution of heat and mass transfer between gas and solid, and it was also included in the dimensionless transport correlations. Literature [29] reports specific surface values up to 21,000 m^{-1} for the 80 ppi foam, suggesting that cracks and pores in the struts connecting the foam cells naturally provide additional surface area.

The specific active catalytic surface, $S_{V,C}$, can differ significantly from the geometrical one, depending on the extent of catalyst dispersion and on the 3D structure of the catalyst on the support. We account for such increase assuming a $S_{V,C} = 16{,}000\ m^{-1}$ [14], in the absence of available measurements. Because of this critical information being assumed, a sensitivity analysis on $S_{V,C}$ was implemented, testing methane conversion and syngas selectivity at $S_{V,C} = 8000$, 16,000 and 32,000 m^{-1}. Analysis was applied to the case of $F = 5$ slpm and C/O = 0.8, where the maximum gap between calculated and experimental data was observed. Results are shown in Table 4 as CH_4 conversion and H_2 and CO selectivity at the catalyst

Table 4
Conversion and selectivities at the exit of the catalyst section for *F* = 5 slpm and the C/O = 0.8 stoichiometry, varying $S_{V,C}$.

	Experimental	$S_{V,C} = 8000\ m^{-1}$	$S_{V,C} = 16{,}000\ m^{-1}$	$S_{V,C} = 32{,}000\ m^{-1}$
X_{CH4} (%)	98.7	84.1	91.7	96.7
S_{H2} (%)	88.8	83.1	89.5	93.3
S_{CO} (%)	93.6	84.8	84.3	83.7

exit. Methane conversion increases at higher $S_{V,C}$, approaching the experimental value at $S_{V,C} = 32{,}000\ m^{-1}$, thus suggesting that the actual catalytic area might have been underestimated by $S_{C,V} = 16{,}000\ m^{-1}$ used in the model. As a matter of fact, the main discrepancies in the species profiles were noted in the reforming zone, where a chemical regime prevails and a correct value of the active catalytic surface is crucial. On the other hand, syngas selectivity does not improve while increasing the active surface area. The H_2 selectivity reaches a value higher than the experimental, while CO selectivity decreases, moving farther to the experimental value. We simply conclude that uncertainties in the $S_{V,C}$ values are not the key to explain the residual discrepancies between model predictions and experimental measurements.

4.5. Sensitivity analysis to the kinetic constants

The evidence that selectivities to syngas are not significantly affected by variation in $S_{V,C}$ suggests that critical steps in the kinetic mechanism, instead of the overall rate, determine the syngas yield. It is out of the scope of this work to suggest a new set of surface kinetic parameters, since it would require a broader and systematic experimental data set. However, sensitivity to kinetic constants can be evaluated. We used the same reference case, i.e. $F = 5$ slpm and C/O = 0.8 stoichiometry. To focus on the kinetic mechanism, a PFR model was implemented using the experimental temperature profile. It corresponds to assuming kinetic regime along the whole reactor. Each pre-exponential factor was individually and independently increased by 10%, and the variation in the CO selectivity at the reactor exit was evaluated. Relative change in S_{CO} was always <1%. Focusing on the reactions (from the mechanism in Table 1) affecting S_{CO} more than 0.1%, we observe that an acceleration of Reactions 1, 3, 9, 10, 13, 15, 23 and 31 increases S_{CO}. Vice versa, increasing the rate of Reactions 4, 6, 7, 12, 14, 16 and 21 lowers S_{CO}. Given these evidence, we tentatively increased by 5% the pre-exponential factor of the reactions that showed a positive selectivity on S_{CO} (i.e. 1, 3, 9, 10, 13, 15, 23 and 31) and decreasing by 5% those with a negative effect. Overall, 15 reaction parameters were modified. The results show an increase by 5.7% in the selectivity for the pure chemical regime simulation described. The modified kinetic mechanism in the complete model, including transport phenomena, leads to an increase in S_{CO} by 6.4%. Results are summarized in Table 5, clearly showing the progress in approaching the experimental measurements. Filling the gap between the model and the experiment was not the aim of this analysis, thus the mechanism was not reformulated further. We reaffirm that even the modifications applied in this analysis are not supported by enough experimental investigation and have to be considered as a mere proof of concept that the kinetics appear to be responsible for the mismatch between calculated and observed product composition. The syngas selectivity is not directly determined by the active catalytic surface-to-volume ratio, and it can be improved by modifying the relative rate of the mechanism, which clearly requires a further refinement.

Table 5
CO selectivity at the exit of the catalyst section for $F = 5$ slpm and the C/O = 0.8 stoichiometry. Results are obtained with a plug flow reactor model using the experimental surface temperature and with a model implementing transport phenomena (this work). The original surface kinetic mechanism was compared with a modified kinetics, where selected reaction rates were altered in order to increase the CO selectivity. The reference experimental value is 93.6%.

	Original kinetics	Modified kinetics (±5% in selected reactions)
PFR (%)	80.9	86.6 (+5.7)
Model (this work) (%)	84.3	89.7 (+6.4)

5. Conclusions

In this work, original experiments at different C/O ratios in the feed and total flowrates are presented and critically compared with model predictions. We developed a pseudo-1D model, including solid, bulk gas and boundary layer mass and energy balances accounting for axial heat conduction and diffusion, and radiation. The micro kinetic model for CH_4 oxidation on Rh, taken from the literature, includes adsorption, desorption and surface reactions.

The experimental data at different stoichiometries show that all product species (H_2, CO, H_2O and CO_2) are formed in the presence of O_2 (oxidation zone) and that both O_2 and CH_4 react in the diffusive regime at C/O = 0.8 and 1, while at C/O = 1.3, the CH_4 reacts already in a mixed regime due to the rather low surface temperatures. In the reforming zone, the slow kinetics produce, at each stoichiometry, a kinetic regime. Increasing the flowrate shifts all species profiles downstream. Besides, their overall shape changes slightly due to changing contributions of convection, diffusion and transport phenomena at different gas velocities. At $F = 10$ slpm, CH_4 conversion is lower despite enhanced mass transfer and higher surface temperatures because the contact time is substantially reduced.

The model reproduces the experimental behavior well, both qualitatively and quantitatively. Best agreement between model and experiments is obtained at the highest C/O. The model describes the oxidation zone generally well for all stoichiometries; however, it underestimates by 10% the exit methane conversion at C/O = 0.8. The results of a sensitivity analysis show that the active catalytic surface-to-volume ratio is likely underestimated in the model. The effect of flowrate is generally well captured by the model apart from in the case of augmented kinetic control. The simulation is excellent at $F = 2.5$ slpm for the entire catalyst length and at higher F in the early oxidation zone, but deviations become larger when surface kinetics become more important. Nonetheless, from the comparison between experimental and calculated data, we concluded that some features of the measured profiles are not reproducible by the model.

The effect of flowrate on the dominant regime was investigated. Pure transport regime and kinetic regime were assumed and the relative resistances calculated and compared, showing that the O_2 reacts in diffusion regime for all the range of F investigated, while CH_4 reacts in transport regime at the lowest F and in mixed regime at the highest.

The model allows analysis of the reaction path leading to hydrogen formation. By inhibition of product re-adsorption in the model, it is demonstrated that H_2 can be a primary product even in the presence of gas phase O_2, supporting the significance of the direct route from CH_4. Both mechanisms, direct and indirect, contribute significantly to produce H_2. One or the other prevails depending on the temperature and the surface coverage of the catalyst.

The analysis of the surface coverages shows an analogous effect when decreasing C/O or increasing F. Mainly because surface temperatures are higher when C/O is decreased or when F is increased, $CO_{(s)}$ and $C_{(s)}$ decrease in coverage while $H_{(s)}$ increases in the steam reforming zone due to a higher rate of the SR reaction. $O_{(s)}$ is consumed in a longer section of the catalyst and $Rh_{(S)}$ increases, meaning that the process becomes more kinetic limited.

Syngas selectivity was also calculated, both from measured and from calculated profiles. S_{H2} is well described by the model at each stoichiometry and flowrate, while S_{CO} is underestimated in every case by up to 8%. A comparison with thermodynamic equilibrium calculations indicates that the experimentally observed CO selectivities are higher on the used Rh catalyst than equilibrium. This is due to the relative slowness of the WGS reaction on this catalyst. On the other hand, those predicted by the model are below

equilibrium, which is the main discrepancy between the model and the experiments. A sensitivity analysis on the kinetic parameters showed that the modification of selected reactions in the surface mechanism enhances the CO selectivity and improves the predictability of the model. Both in the measured and in the calculated profiles, CO_2 is produced in the oxidation zone and also in the reforming zone only in the case of C/O = 0.8. In this test, the catalyst temperature is above 800 °C, and the WGS reaction is kinetically favored; this indicates that continued CO_2 formation can be avoided if the catalyst temperature is kept below this value.

References

[1] S.G. Brass, G. Ehrlich, J. Chem. Phys. 87 (1987) 4285.
[2] A.B. Mhadeshwar, D.G. Vlachos, J. Phys. Chem. B 109 (2005) 16819.
[3] M. Maestri, D.G. Vlachos, A. Beretta, G. Groppi, E. Tronconi, AIChE J. 55 (2009) 993.
[4] D.A. Hickman, L.D. Schmidt, AIChE J. 39 (1993) 1164.
[5] R. Schwiedernoch, S. Tischer, C. Correa, O. Deutschmann, Chem. Eng. Sci. 58 (2003) 633.
[6] B.C. Michael, A. Donazzi, L.D. Schmidt, J. Catal. 265 (2009) 117.
[7] A. Donazzi, A. Beretta, G. Groppi, P. Forzatti, J. Catal. 255 (2008) 241.
[8] A. Donazzi, A. Beretta, G. Groppi, P. Forzatti, J. Catal. 255 (2008) 259.
[9] A. Donazzi, B.C. Michael, L.D. Schmidt, J. Catal. 260 (2008) 270.
[10] D.G. Loffler, L.D. Schmidt, AIChE J. 21 (1975) 786.
[11] S.T. Kolaczkowski, Catal. Today 47 (1999) 209.
[12] L.D. Pfefferle, Catal. Today 26 (1995) 255.
[13] L.L. Raja, R.J. Kee, O. Deutschmann, J. Warnatz, L.D. Schmidt, Catal. Today 59 (2000) 47.
[14] D. Dalle Nogare, R. Horn, N.J. Degenstein, P. Canu, L.D. Schmidt, J. Catal. 258 (2008) 131.
[15] D. Wolf, M. Hohenberger, M. Baerns, Ind. Eng. Chem. Res. 36 (1997) 3345.
[16] R. Horn, K.A. Williams, N.J. Degenstein, L.D. Schmidt, J. Catal. 242 (2006) 92.
[17] M. Bizzi, G. Saracco, R. Schwiedernoch, O. Deutschmann, AIChE J. 50 (2004) 1289.
[18] M. Maestri, A. Beretta, G. Groppi, E. Tronconi, P. Forzatti, Int. J. Heat Mass Transfer 105 (2005) 709.
[19] M. Bizzi, L. Basini, G. Saracco, V. Specchia, Chem. Eng. J. 90 (2002) 97.
[20] M. Bizzi, L. Basini, G. Saracco, V. Specchia, Ind. Eng. Chem. Res. 42 (2003) 62.
[21] N.V. Vernikovskaya, L.N. Bobrova, L.G. Pinaeva, V.A. Sadykov, I.A. Zolotarskii, V.A. Sobyanin, I. Buyakou, V. Kalinin, S. Zhdanok, Chem. Eng. J. 134 (2007) 180.
[22] R. Horn, K.A. Williams, N.J. Degenstein, L.D. Schmidt, Chem. Eng. Sci. 62 (2007) 1298.
[23] N.J. Degenstein, Dep. of Chemical Engineering and Materials Science, University of Minnesota, Ph.D. Thesis, 2007.
[24] S.R. Turns, An Introduction to Combustion: Concepts and Application, second ed., McGraw-Hill, 2000.
[25] R. Horn, K.A. Williams, N.J. Degenstein, A. Bitsch-Larsen, D. Dalle Nogare, S.A. Tupy, L.D. Schmidt, J. Catal. 249 (2007) 380.
[26] C. Appel, J. Mantzaras, R. Schaeren, R. Bombach, A. Inauen, N. Tylli, M. Wolf, T. Griffin, D. Winkler, R. Carroni, Proc. Combust. Inst. 30 (2005) 2509.
[27] S. Eriksson, M. Wolf, A. Schneider, J. Mantzaras, F. Raimondi, M. Boutonnet, S. Järås, Catal. Today 117 (2006) 447.
[28] R. Horn, N.J. Degenstein, K.A. Williams, L.D. Schmidt, Catal. Lett. 110 (2006) 169.
[29] M.V. Twigg, J.T. Richardson, Chem. Eng. Res. Des. 80 (2002) 183.
[30] S. Tischer, C. Correa, O. Deutschmann, Catal. Today 69 (2001) 57.
[31] O. Deutschmann, L.D. Schmidt, AIChE J. 44 (1998) 2465.
[32] C.T. Goralski Jr., R.P. O'Connor, L.D. Schmidt, Chem. Eng. Sci. 55 (2000) 1357.
[33] G. Veser, J. Fraunhammer, Chem. Eng. Sci. 55 (2000) 2271.
[34] F.P. Incropera, D.P. DeWitt, Fundamentals of Heat and Mass Transfer, fifth ed., Wiley, New York, 1996.
[35] J.G. Fourie, J.P. Du Plessis, AIChE J. 50 (2004) 547.
[36] R.J. Kee, M.E. Coltrin, P. Glarborg, Chemically Reacting Flow: Theory and Practice, John Wiley & Sons, Inc., New York, 2003. 77, 89, 99, 467–472.
[37] D.G. Goodwin, An open-source, extensible software suite for CVD process simulation, in: M. Allendorf, Maury, F. Teyssandier (Eds.), Proceedings of CVD XVI and EuroCVD Fourteen, Electrochemical Society, 2003, p. 155.
[38] Matlab, MathWorks.
[39] GRI-Mech 3.0. <http://www.me.berkeley.edu/gri-mech>.
[40] H. Scott Fogler, Elements of Chemical Reaction Engineering, fourth ed., Prentice-Hall, 2005.
[41] H. Heitnes Hofstad, J.H.B.J. Hoebink, A. Holmen, G.B. Marin, Catal. Today 40 (1998) 157.
[42] I. Tavazzi, A. Beretta, G. Groppi, P. Forzatti, J. Catal. 241 (2006) 1.
[43] M. Maestri, Dipartimento di chimica, materiali e ingegneria chimica, Politecnico di Milano, Ph.D. Thesis, 2008.